Migration Letters

Volume: 20, No: S6 (2023), pp. 1247-1284

ISSN: 1741-8984 (Print) ISSN: 1741-8992 (Online)

www.migrationletters.com

Photodegradation Of Industrial Dyes Using Graphene/Zinc-Codoped Fe_3o_4 Nanocomposites Prepared By The Coprecipitation Technique Is Assisted By Uv Light

J.F.Joe Sherin[a], G.Edwin Sheela[a*]

Abstract

Industrial dye waste is extremely harmful to the environment, nonbiodegradable, and poisonous to a high degree. Fe_3O_4 nanoparticles (F-NPs), graphene-doped Fe_3O_4 nanocomposites (G/F-NCs), zinc-doped Fe_3O_4 nanoparticles (Zn/F-NPs), and graphene-zinc codoped Fe_3O_4 nanocomposites (G/Zn/F-NCs) are all capable of photodegrading phenothiazine derivative dyes. The X-ray powder diffraction patterns of each manufactured sample support the face-centered cubic structure of metallic Fe_3O_4. While the inclusion of graphene dopants causes a reduction in particle size and an expansion of the bandgap, the Zn-doped samples show an increase in crystallite size, showing that Zn 2p considerably encourages the growth of crystalline grains in Fe_3O_4. The formation of secondary pores and the incorporation of graphene nanoflakes are responsible for the increased specific surface area of G/Zn/F-NCs (71.115m^2/g). The oxygen anions, graphene, Zn 2p ions and Fe_3 and Fe_2 oxidation states are all present in the Fe_3O_4 lattice, according to the X-ray photoelectron spectra of O 1s, C1s, Zn 2p and Fe 2p.

Keywords: *graphene-zinc codoped Fe_3O_4 nanocomposites; XRD; XPS; EDAX*

1.Introduction

The two most pressing problems in the modern world are environmental deterioration and the energy problem. Among the most significant problems the energy storage sector is the production of energy from inexpensive materials. However, industrial water contamination is a significant environment[1]al problem. The majority of industrial waste in affluent nations contains significant amounts of xenobiotic composites (dyes) are used. In these hazardous for animals, humans, and aquatic species, difficult to biodegrade, and recalcitrant (VanHuyNguyen et al., 2020). The thyazine dyes can be described as heterocyclic series because of the presence of nitrogen and sulphur. The current case specifically considers Methylene Blue (MB), a thyazine dye (medicine dye) that is commonly found in industrial waste-water due to its substantial side effects and detrimental impacts on the environment (Chandra et al., 2010). So it's crucial to remove commercial water dye using affordable and environmentally acceptable materials. Due to their many physicochemical features, magnetite (Fe_3O_4) nanoparticles have

[a]Research Scholar (Register No. 20113232132005), Department of Physics, Muslim Arts College, Thiruvithancode-629174, Affiliated to Manonmanium Sundaranar University, Abishekapatti, Tirunelveli-627 012, Tamilnadu, India.
[a*]Department of Physics, Muslim Arts College, Thiruvithancode, Kanyakumari District-629174, Tamilnadu, India.

generated a lot of interest in the research community over the past few years. Magnetic nanoparticles of iron oxides are undergoing intensive research due to their biocompatibility, high oxidative stability, magnetic property, and chemical strength. Fe_3O_4 nanoparticles have a wide range of applications, including those for MRI contrast agents, metal ion absorbents in water treatment, drug delivery, hyperthermia therapy, medical diagnostics, and the treatment of cancer (Dubus et al., 2006; Kim et al., 2010; Liu et al., 2020; Bharath et al., 2022; Kim et al.,2005; Chang et al.,2005; Setiadi et al., 2017; Beji et al.,2010; Gautam et al., 2017).

One of the strongest magnetic nanoparticles is magnetite, or Fe_3O_4. An extensively researched ferrimagnetic oxide with a cubic inverse spinel structure is Fe_3O_4. Fe_3O_4 is the main mineral found in iron sand (Jalil et al., 2017; Riana et al., 2018). The electron hopping between the Fe^{2+} and Fe^{3+} ions in the octahedral sites gives it its magnetic and electric characteristics. It is common knowledge that adding transition metal ions to Fe_3O4 can increase its catalytic activity (Mahdavi et al., 2013). The ferrimagnetic oxide Fe_3O_4, which possesses an inverse cubic spinel structure, has been extensively researched. Due to the electron hopping between Fe^{2+} and Fe^{3+} ions in the octahedral positions, it possesses magnetic and electric characteristics. Adding transition metal ions to Fe_3O_4 can increase its catalytic activity, which is a well-known technique (Mahdavi et al., 2013). By adding rare earth or transition metal elements to Fe_3O_4 (Tsai et al., 2004; Chen et al., 2005; Penc et al., 1999; Li et al., 2004), it is possible to enhance the magnetic performance of this material. Thin film samples of Fe_3O_4 are studied, and the doping process normally impacts the associated magnetite-based materials' structural, magnetic, and transport aspects (He et al., 2013; Tripathy et al., 2007; Takaobushi et al., 2007; Moyer et al., 2011; Chou et al., 2005). There are numerous techniques for creating magnetic Fe_3O_4 nanoparticles, including hydrothermal synthesis, thermal decomposition, micro-emulsion, co-precipitation, sol-gel, thermal treatment, solvothermal, combustion, ceramic method, soft mechanochemical method, sonochemical, and microwave-assisted synthesis (Amara et al., 2009; Agusu et al., 2019; Hu et al., 2006; Hu et al., 2007; Hong et al., 2006; Naseri et al., 2011; Yadav et al., 2017; Agusu et al., 2019; Lazarevic et al., 2013; Deng et al., 2005; Xu et al., 2009; Tang et al., 2004; Laurent et al., 2008; Matijevicet al., 1975).

Due to their biocompatibility and high saturation magnetization, Fe_3O_4 nanoparticles have been the subject of extensive research over the past several decades (Qiao et al., 2009; Yang et al., 2009; Lu et al., 2007; Laurent et al., 2008). These properties make them suitable for a variety of biomedical applications. In the remediation of ground water, particularly for the removal of arsenic, Fe_3O_4 has established application for the separation of water contaminants. According to Deng et al. (2005), the co-precipitation method is an alkali medium reaction in which stoichiometric mixes of ferrous and ferric hydroxides create copious amounts of Fe_3O_4 nanoparticles. According to Yang et al. (2011), this approach is distinguished by its low temperature, quick reaction time, and high reaction yield. According to Liu et al. (2019), Fe_3O_4 nanoparticles indicate higher SA:V leading to superior paramagnetic activities, which in turn increases the technique a process of breakdown by reducing the strong dipolar attraction and surface energy of nanoparticles. Fe_3O_4 is therefore well regarded as a important ingredient for photocatalysis because of its inexpensive cost, highly sensitive surface, high electron transfer rate, and excellent adsorption effectiveness against harmful water pollutants. These properties also support an appropriate for the treatment or removal of nanocomposites, magnetic separation with an external magnet (Balamurugan et al., 2019) (Liu et al., 2019). Surface characteristics, bonding efficiency, lattice flaws, and electronic and lattice structure can all have a significant impact on a transition metal oxide's photocatalytic efficacy (Balamurugan et al., 2019; Liu et al., 2019). In recent years, cation doping into iron oxide has become widely used to modify the physical and chemical characteristics of Fe3O4 nanoparticles, such as the strength of the link between the metal and oxygen, bulk defect, lattice

structure, etc., and hence improve the performance of catalysts and energy storage systems (Liu et al., 2019; Bharath et al., 2022).

According to Vedernikova et al. (2013) and Hu et al. (2007), zinc is a member of a class of microelements and is important for many crucial biochemical reactions and physiological activities, including cell development and growth. In terms of the d-block elements, zinc is the second most abundant in the human body after iron, and its deficiency can lead to oxidative stress and DNA damage (Zyba et al., 2017; Ho et al., 2002). Another metal that is extensively employed in the sector is zinc. One of the most frequently used elements to dope into Fe_3O_4 is Zn (Gupta et al., 2002; Wen et al., 2006; Srivastava et al., 1976; Srivastava et al., 1976; Lu et al., 2006). (Gupta et al., 2002; Wen et al., 2006; Srivastava et al., 1976; Lu et al., 2006). One of the metal substitutes that improves the performance of the Fe_3O_4 particles is zinc (Zn). When it comes to doping Fe_3O_4 nanoparticles, Zn^{2+}, which has the same ionic radii as Zn and Fe, is the most effective transition metal ion. In order to stabilise the phase, Zn^{2+} ion can therefore easily replace Fe^{3+} ion in the Fe_3O_4 lattice without affecting the crystal structure (Anjana et al., 2018). Zn^{2+} is essential for the human body to operate properly, and its involvement in complex enzymatic reactions and food fortification with Zn^{2+} demonstrate this (Eide et al., 2011). For magnetic ferrite NPs, Zn^{2+} would be a biocompatible dopant. According to a recent study (Anjana et al. 2018), Zn-doped magnetite exhibits higher antibacterial activity than pure magnetite nanoparticles. The Zn level may also alter the Zn-doped magnetite ferrofluids' magnetic, structural, and particle-size characteristics, which could alter how well they fight bacteria. Therefore, a thorough investigation into the change of Zn composition is necessary to arrive at a suitable composition for enhancing the antibacterial activity of Zn-doped magnetite. According to Su et al. (2012), zinc ferrite ($ZnFe_2O_4$), one of the spinel ferrites, has garnered considerable interest in the photo-catalytic remediation of pollutants. The intrinsic peroxidase-like activity of $ZnFe_2O_4$ causes it to react with H_2O_2 to create OH (Liu et al., 2014).

According to Balamurugan et al. (2018), graphene is regarded as the most in-demand substance in the research sector because of its distinctive properties and wide range of uses as adsorbents, active material in the fabrication of supercapacitor electrodes, materials for thermal transmission as well as biosensor components. The conductivity, theoretical surface area ($2600 m^2/g$), chemical strength, and thermal stability of the material can all be improved by adding graphene (Balamurugan et al., 2016; Chen et al., 2019 Vijayalakshmi et al., 2021; Vermisoglou et al., 2019; Ng et al., 2017). The efficiency of several energy conversion, storage, and catalytic reactions would therefore be improved by the coupling of metal oxides with graphene (Wu et al., 2010; Ashraf et al., 2021). Fe_3O_4 nanoparticles can be made using a wide range of preparation techniques, including the sonochemical technique, sol-gel technique, microemultion, electrospray technique, flow injection technique, hydrochemical procedure, and co-precipitation methodology (Liang et al., 2020; Hosseini et al., 2013; Anjana et al., 2018). Due to its low cost, environmental friendliness, high product yield and purity, and reproducibility, the co-precipitation approach has become one of the most used synthesis techniques (Athar et al., 2015; Cruz et al., 2018).

In addition to being a single layer of carbon atoms, graphene (G) belongs to a brand-new class of carbon-based nanomaterials. Due to its exceptional electric, thermal, and mechanical properties, graphene has recently gained a lot of attention from researchers in the field of nanotechnology (Geim et al., 2007). Based on these properties, it has an applications in several areas, such as molecular probes (Wang et al., 2010; Lin et al 2011), electrochemical sensors (Tang et al., 2009; Wang et al., 2010; Wang et al., 2012; Wang et al., 2012) nanocomposites (Wang et al., 2010; Wang et al., 2012) adsorbents, supercapacitor electrode active material, electrical components, and thermal transport media (Simeonidis et al., 2007;

Zhou et al., 2008). According to a number of studies, (Han et al., 2012; Zhang et al., 2013; Zhao et al., 2011), graphene may be a better choice for use as an adsorbent for the extraction of compounds with benzenoid structures because it possesses several delocalized electron systems that can form a solid stacking contact with benzene rings. The "scotch tape" method was used to first obtain it in a lab setting (Novoselov et al., 2004). Due to its exceptional properties, including as its large specific surface area, outstanding mechanical rigidity, extraordinary electrical transport, and great biocompatibility, graphene is an ideal material for electrode modification (Yang et al., 2010). The hydrophobic nature of graphene, however, prevents it from functioning properly in water. Aftabtalab et al. (2015) and Giraldo et al. (2013) found that rGO has promising potential as a porous material for seawater desalination, which removes a variety of water pollutants including metallic ions, anions, microplastics, nanoparticles, organic chemicals, and biological substrate. Graphene can be changed into graphene oxide (GO) by oxidising it (Zhao et al., 2015; Lee et al., 2015) in order to enhance its dissolving property. In order to create reduced graphene oxide (rGO), reducing agents are used to convert graphene oxide into the material (Mussa et al., 2020). Although there are numerous graphene-like properties, it might have some oxygen-containing groups on the surface. According to Sharma et al. (2017), rGO sheets are a kind of graphene that was produced chemically.

According to Perreault et al. (2015) and Gurunathan et al. (2013), the bioactivity of graphene-based materials was based on surface contact and was produced by the production of reactive oxygen species (ROS). Graphene and graphene mixed with IONPs have been used in the current context, and the results have been reported (Santos et al., 2012; Pelin et al., 2017; Hastak et al., 2018; Yang et al., 2019; Jedrzejczak et al., 2017; Gade et al., 2015). Graphene with Fe_3O_4 was studied by Jedrzejczak-Silicka et al. in 2017 for its impact on DNA integrity and relative viability. In conclusion, they noted that the material had high biocompatibility and that it might be used to treat hyperthermia. According to Wang et al. (2012) and Yao et al. (2012), Fe_3O_4/graphene composites have attracted a lot of attention for their ability to enhance transfer and adsorption capabilities. Since the creation of a synergistic effect could be expected to have high potential in lithium ion batteries, microwave-absorbing materials, biomedicine, and supercapacitors, graphene/Fe_3O_4 composite film has received particular attention (Zhou et al., 2010; Zhang et al., 2014; Ou etval., 2014; Liu et al., 2014). Purified rGO/Fe_3O_4 nanoparticle dispersion synthesised from chemical reduction technique (Liang et al., 2010) was used to create films based on graphene. For prospective use as magnetically controlled switches, graphene/F-NP hybrid films demonstrated superparamagnetic characteristics. The Fe_3O_4 is effectively electrically connected to the reduced graphene oxide, enhancing conductivity and minimising Fe_3O_4 loss brought on by volume fluctuations during discharge/charge processes. By using a hydrothermal technique, (Cunqing et al., 2017) created a Fe_3O_4/graphene nanosheet composite. Fe_3O_4/rGO nanocomposites are photocatalytically active materials (Peik et al., 2014; Padhi et al., 2017), for decreasing heavy metals such the ions of Cu^{+2}, Zn^{+2}, and Ni^{+2} (Moradinasab et al., 2016), Cr^{-2}, Pb^{2+}(Cao et al., 2015; Wang et al., 2015; Sun et al., 2014; Al et al., 2016), detecting Cd^{+2} (Yu et al., 2014) ions, degradation of phenol, antibacterial (Padhi et al., 2017), biosensing (Yu et al., 2014) and absorbent for withdrawing dyes in aqueous solutions (Yang et al., 2015 ; Yang et al., 2018; Namvari et al., 2014). In mineral water (Cui et al., 2012; Chimezie et al., 2017) and waste water treatment (Mahalingam et al., 2018), it may be incorporated into a sensor to identify the presence of arsenic. A photo-Fenton-type reaction may occur when graphene and Fe3O4 are combined, creating an effective, non-toxic, and environmentally safe mechanism for the breakdown of industrial dyes.

Because a photodegradation process considerably reduces pollutants and produces harmless end products (CO_2 and H_2O), it has been utilised to clean industrial waste water (Gupta et al., 2012). Since many years ago, iron oxides have been the subject of extensive research due to their nontoxicity, high efficacy, stability, and high activity under continuous use (Chin et al., 2007, Mandal et al., 2015; Yavuz et al., 2006). The huge surface area ($2600 m^2/g$), superior mechanical flexibility, and optical transparency of graphene functionalized nanocomposites have been reported to greatly improve the photodegradation properties (Gupta et al., 2012). In order to effectively remove natural colours, heavy metal ions, and pesticides from river sand, graphene is attached to the surface of the sand (Gupta et al., 2012). According to research on waste water treatment by Kami et al. (2022), graphene-Fe_3O_4 has been reported to photodegrade contaminants. The synthesis of Fe_3O_4 with graphene provides the possibility to use like a photo-Fenton response to breakdown industrial dyes in a way that is efficient, nontoxic, and environmentally acceptable. The degradation of coloured pigments by zinc along with Fe_3O_4 that is doped with graphene has not been thoroughly studied. As a result, it is anticipated that double doping Fe_3O_4 with both zinc (Zn) and graphene (G) will produce better results than either undoped or single element doped Fe_3O_4. In this instance, the degradation of an industrial dye was evaluated using Zn and G as dopants on Fe_3O_4.

2.Experimental

2.1Materials

The 30% ammonia solution (NH_3), ferric chloride hexahydrate ($FeCl_3.6H_2O$), and ferrous chloride tetrahydrate ($FeCl_2.4H_2O$) were bought from National Scientific Company in Madurai. We bought zinc sulphate $ZnSO_4.7H_2O$ and graphene from Sigma-Aldrich. From Himedia Laboratories Pvt. Ltd., washable reagents were acquired. Deionized water was used to make each and every aqueous solution. Without additional purification, all of the materials utilised in this investigation were of analytical quality.

2.2 Preparation of nanocomposites

Synthesis of Fe_3O_4 nanoparticles (F-NPs), graphene-doped Fe_3O_4 (G/F-NCs), zinc-doped Fe_3O_4 (Zn/F-NPs) and graphene-zinc codoped Fe_3O_4 (G/Zn/F-NCs) nanocomposites

Fe_3O_4 nanoparticles were created using 0.07 M $FeCl_2.4H_2O$ and 0.14 M $FeCl_3.6H_2O$ in deionized water with constant stirring, they were dissolved in a 1:2 molar ratio (Maity et al., 2007; Arakha et al., 2015; Ramanathan et al., 2021). The aforementioned homogenous solution was added dropwise with a 30% ammonia solution, and the temperature was held at that level for an hour while vigorous stirring. A pH metre was used to determine the pH of the solution, which was 7. A black coloured precipitate was produced as a result of the response. The precipitate was collected, three distilled water washes were performed and then calcined for one hour at 300°C. The prepared sample also included the designation "F-NPs." Using the equation shown below, the entire method may be discussed:

$$FeCl_2 + FeCl_3 + 8NH_3 + 4H_2O \rightarrow Fe_3O_4 + 8NH_4Cl$$

0.05 g of graphene was added to the initial homogeneous solution to create the graphene doped Fe_3O_4 nanocomposite and the identical steps regarding the F-NPs repeated. And G/F-NCs was the designation given to the prepared sample.

The initial homogeneous solution was mixed with 0.09 g of zinc sulphate $ZnSO_4.7H_2O$ to create the zinc doped Fe_3O_4 nanocomposite. The procedure was then repeated to create F-NPs. And Zn/F-NPs were used to identify the produced sample.

Following the same procedure as for F-NPs, 0.05 g of graphene with 0.09 g of zinc sulphate $ZnSO_4.7H_2O$ were included into the original homogenous solution to produce graphene and zinc double doped Fe_3O_4 nanocomposite. The prepared sample had the designation G/Zn/F-NCs on it. Further characterizations were performed on the acquired product. In Fig. 1, a schematic representation of the creation of F-NPs, G/F-NCs, Zn/F-NPs, and G/Zn/F-NCs is shown.

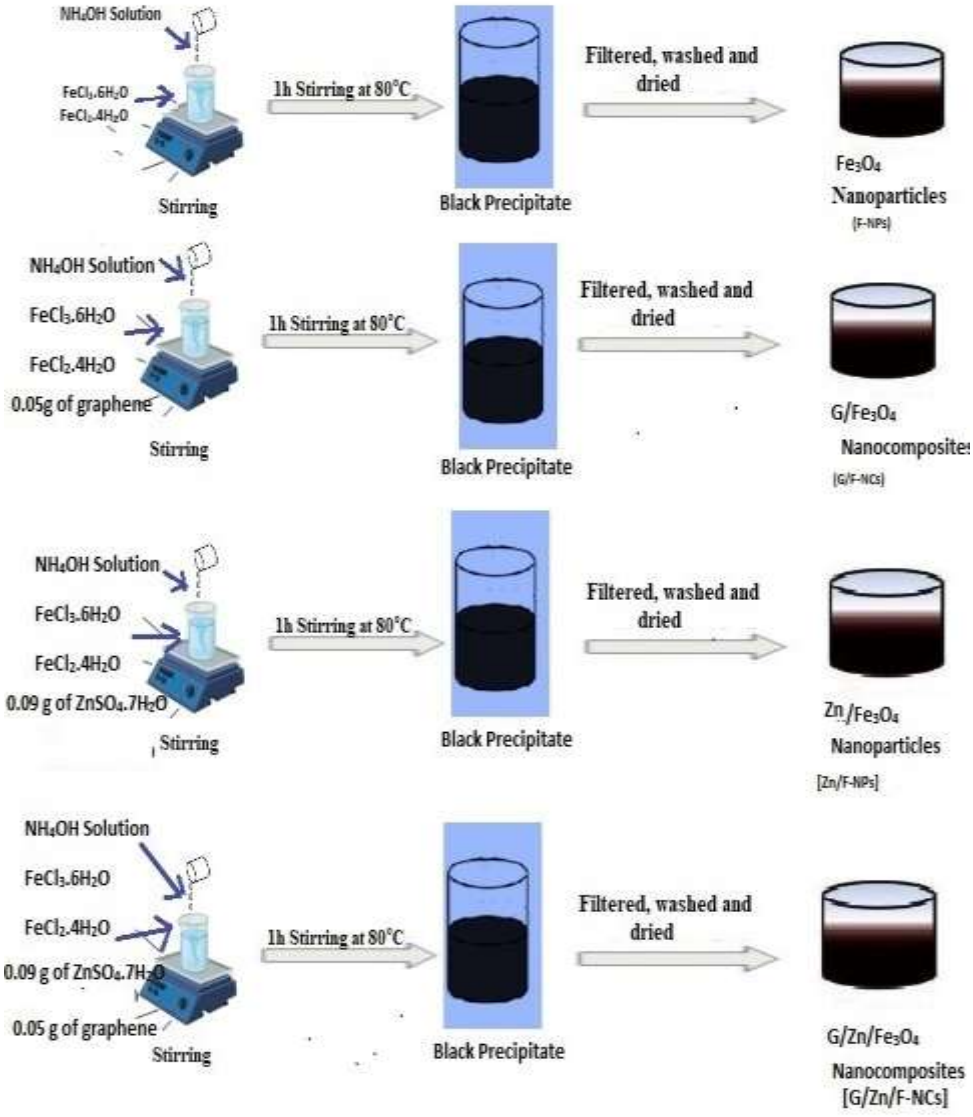

Fig. 1: Synthesis of F-NPs, G/F-NCs, Zn/F-NPs and G/Zn/F-NCs

2.3 Instrumentation

With the use of a powder X-ray diffraction apparatus using Cu K radiation (= 0.15406 nm), the crystal structure of the produced nanomaterials was investigated. The oxidation states of the materials were investigated using X-ray photoelectron spectroscopy (XPS) investigations using

a PHI 5000 Versa Probe II (purchased from ULVAC-PHI Inc., USA) equipped with a microfocused (200 m, 15 KV) monochromatic Al-K X-Ray source (hv = 1486.6 eV). Using UV-visible and photoluminescence (PL) spectroscopy, the optical characteristics of the produced nanoparticles are examined. In order to examine vibrations, Fourier Transform Infrared Spectroscopy (FT-IR) was performed using a Shimadzu FT-IR spectrophotometer. Scanning electron microscopy (EOL JSM-5600 LV) was used to take images of the sample's surface and map its elements. A study of the synthesised sample's elemental makeup using energy dispersive spectroscopy (EDAX) was done. Transition electron microscopy and a selected area electron diffraction pattern (SAED) (FEI, TECNAI S twin microscope with a 100 KV acceleration voltage) were used to examine the material's microstructure and particle size. Altamira Instruments, Inc.'s (BET) Brunauer Emmet Teller (2 nm-500 nm, macro and mesopore analysis) N_2, Ar are adsorbents. The BET surface area adsorption and desorption isotherms of the material were examined using degassing temperatures up to 350° C.

The antibacterial F-NPs, G/F-NCs, Zn/F-NPs and G/Zn/F-NCs activity against Pseudomonas aeruginosa and Staphylococcus aureus was assessed using the disc diffusion method. To raise the culture up to McFarland standards (108 CFC/mL), all samples were inoculated into sterile nutrient broth (Hi Media) (1.5 mL) and grown for two hours. Utilising a sterile spreader, the inocula were applied to brand-new nutrient agar plates. The selected centre received the control disc. Each individual organism appeared three times on the Mueller-Hinton-Agar/Hi Media after 100 L of revived culture were dispersed over it. All of the prepared samples (50 L) were placed in a single 4 mm-diameter well. After 24 hours at 37 °C in an incubator with all the petri plates, the zones of inhibition (ZOI) were assessed in millimetres.

The photocatalytic function of F-NPs, G/F-NCs, G/Zn/F-NCs and Zn/F-NPs was measured using a UV-vis spectrophotometer (Systronics 2203, India). In order to assess the breakdown of the dye under UV light, with a pH of 8, 8 mg L^{-1} of methylene blue (MB) dye was combined with 0.9 mg L^{-1} of an aqueous solution of the catalysts that were created.

3. Results and Discussion

3.1 Structural Studies (XRD)

Fig. 2 shows the XRD patterns of F-NPs, G/F-NCs, Zn/F-NPs, and G/Zn/F-NCs. In the F-NPs XRD pattern, the diffraction peaks are indexed as 18.54° (111), 30.32° (220), 35.73° (311), 43.01° (400), 53.41° (422), 57.16° (511) and 62.85° (440). In order to identify the G/F-NCs' diffraction peaks, the XRD pattern at 30.41° (220), 35.47° (311), 43.23° (400), 53.37° (422), 56.97° (511) and 62.63° (440). The presence of the graphene (002) peak in G/F-NCs implies the creation of G/F-NCs nanocomposites. The diffraction peaks at 18.39° (111), 30.25° (220), 35.02° (311), 42.37° (400), 52.28° (422), 56.84° (511) and 62.39° (440) are indexed according to the XRD pattern of Zn/F-NPs. The peaks with Zn doping were somewhat offset to lower angles in comparison to pure F- NPs, showing that the Fe_3 and Fe_2 ions in the Fe_3O_4 lattice had been switched out for the ions of Zn. Production of Zn/F- NPs was most advantageous since both iron and zinc ions could easily occupy their desired positions. The peaks at 30.13° (220), 35.55° (311), 42.43° (400), 53.25° (422), 56.67° (511) and 62.71° (440) are indexed according to the G/Zn/F-NCs' XRD pattern. According to Cheng et al. (2017), the G/Zn/F-NCs' XRD pattern showed a tiny peak at 24.3° in agreement with graphene's (002) reflection. These findings suggest that the Fe_3O_4 crystal phase in the G/Zn/F-NCs was unaffected by the graphene addition. These are the reflections of Face Centred Cubic (FCC) Fe_3O_4 nanoparticles from the JCPDS file No. 65-3107 (Anjana et al.,2018).

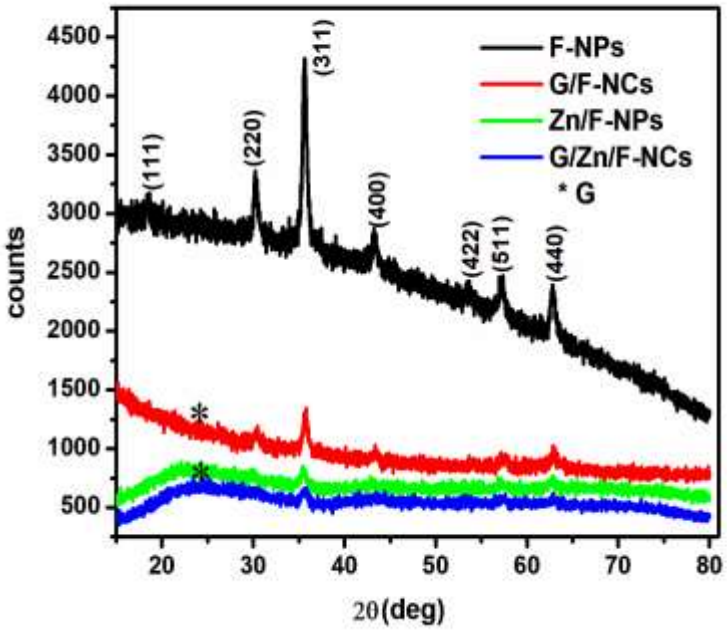

Figure 2 shows the X-ray diffraction pattern for F-NPs, G/F-NCs, Zn/F-NPs and G/Zn/F-NCs

The crystalline size, cell volume, lattice constant, strain, bond length on the octahedral, tetrahedral, and cubic spinel sites, as well as the dislocation density of F-NPs, G/F-NCs, Zn/F-NPs and G/Zn/F-NCs are listed in Table 1. The approximate crystalline diameters of F-NPs, G/F-NCs, Zn/F-NPs and G/Zn/F-NCs were 34.22 nm, 38.61 nm, 41.58 nm, and 40.73 nm, respectively, according to Scherrer's equation. According to the calculated crystallite size, Zn/F-NPs give a larger size than F-NPs. The prepared Zn/F-NPs appear to have high crystallinity based on the strong, crisp peaks (Farimani et al., 2013). According to theory, this increase was brought on by a rise in Zn^{2+} concentration, which has a larger ionic radius than Fe^{2+} and Fe^{3+} (Mozaffari et al. 2015). Calculated lattice parameters for F-NPS, G/F-NCs, Zn/F-NPs, and G/Zn/F-NCs were 8.3880, 8.3845, 8.3814, and 8.3827, respectively. With a value of 8.396, they are significantly less than that of bulk matter. The construction of nanoparticles is the result of the interior atoms being compressed into the spherical bodies (Sun et al., 2006). Due to the modest variation in the ionic radii of Zn (0.74) and Iron (0.645), the observed lattice parameter of pure and doped F-NPs does not demonstrate a significant difference (Anjana et al., 2018). Additionally, it has been found that the lattice parameter marginally decreases as Zn^{2+} level rises (Ramesh et al., 2019). The lattice parameter and cell volume values obtained are reasonably close to the values (a=8.390, V = 590.70 3) in JCPDS file number 65-3107. The values of cell volume have a similar tendency to those of lattice constants since they closely correlate with each other (Somvanshi et al., 2020). The variation in the I220/I440 values, according to Lassoued et al. (2018), can be utilised to explain the cations at the tetrahedral and octahedral sites.

Table 1: Structural parameters of XRD analysis

Sample	Grain size (D) (nm)	Lattice parameter (a) (A°)	Dislocation density (δ) (m^{-2})	Cell volume (V) ($A°^3$)	Strain	Hopping length (L_A) (A°)	Hopping length (L_B) (A°)	X-ray density (d_x) (gm/cm^3)	Tetrahedral bond length (d_{AX}) (A°)	Octahedral bond length (d_{BX}) (A°)	Surface area (m^2/g)	Pore Volume (cm^3/g)	Pore size (nm)
F-NPs	34.22	8.3880	0.00085	590.17	0.0087	3.6327	2.9660	5.2119	1.8161	2.097	48.742	0.168	13.766
G/F-NCs	38.61	8.3845	0.00069	589.43	0.00099	3.6322	2.9648	5.2185	1.8153	2.0961	69.798	0.126	7.197
Zn/F-NPs	41.58	8.3814	0.00048	582.84	0.00091	3.6311	2.9612	5.3035	1.8042	2.0924	49.514	0.165	13.517
G/Zn/F-NCs	40.73	8.3827	0.00051	583.39	0.00097	3.6315	2.9626	5.2854	1.8099	2.0932	71.115	0.244	13.747

By using X-ray photoelectron spectroscopy (XPS), the oxidation states of the produced G/Zn/F-NCs are determined. The survey spectrum of G/Zn/F-NCs in Fig. 3(a) demonstrates that oxygen, zinc, and iron components are present in the final product. Graphene is another component of the synthesised material that contributes to the carbon peak's presence. Atomic percentage of elements detected by XPS analysis Fe of 27.12%, O of 46.97%, C of 25.61%, Zn of 0.1%. As seen in the inset, two strong peaks brought on by $2p_{3/2}$ are visible in the high-resolution XPS spectra of Fe 2p (Fig. 3(b)) (at a wavelength of around 711.39 eV) and $2p_{1/2}$ (at a wavelength of around 725.21 eV) (Wu et al., 2015; Zhang et al., 2016). Deconvolution of the $2p_{3/2}$ peak reveals two peaks related to Fe^{2+} (at 711.05 eV) and Fe^{3+} ions (at 712.98 eV). Deconvolution of the $2p_{1/2}$ peak can also reveal the presence of two peaks brought on by Fe^{2+} and Fe^{3+}ions that are present in the Fe_3O_4 lattice, respectively at 732.73 eV and 725.54 eV (Wang et al., 2012; Chen et al., 2013). Two peaks at 1025.20 and 1048.76 eV in the high-resolution XPS spectrum of Zn 2p, which are attributed to Zn $2p_{3/2}$ and Zn $2p_{1/2}$, respectively, imply the existence of Zn^{2+} in the Fe_3O_4 products (Liu et al., 2015; Li et al., 2014; Yu et al., 2019). From the high resolution XPS spectrum of the C1s level (Fig. 3(d)), four peaks could be identified. Graphene-like sp^2 hybridised carbon is responsible for the largest peak at 284.75 eV. According to Chang et al. (2013), the different surface oxidation states C-O, C=O, and O-C=O are responsible for the peaks at 285.54, 288.62, and 293.28 eV, respectively. The O anions in the Fe3O4 lattice are identified as the three peaks in the high-resolution O1s spectra (Fig. 3(e)), with the peak at 530.38 eV being the most obvious. The graphene in the composite establishes surface bonds with oxygen at 531.86 and 532.78 eV, while at 532.78 eV, the oxygen in the Fe-OH group contaminates the surface of the Fe3O4 particles. The spectra's high binding energy region may be influenced by numerous more smaller peaks, which is usually due to surface flaws, impurities, and chemisorbed oxygen species. In spite of this, it is clear from the spectra that their existence, if any, would be too negligible to have a substantial impact on the current investigation (Wang et al., 2012).

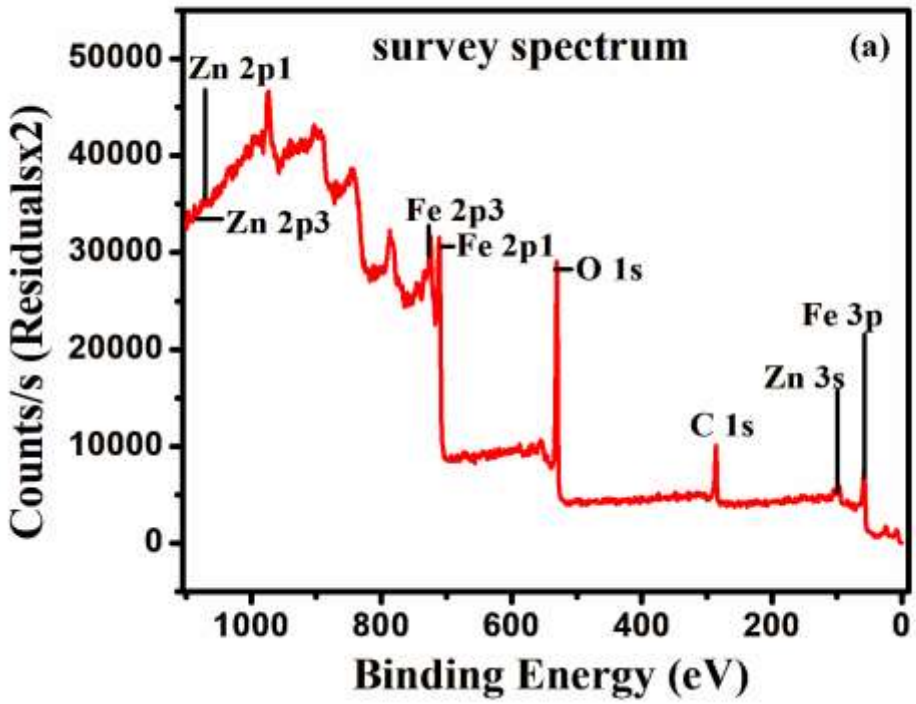
survey spectrum
(a)
Zn 2p1
Zn 2p3
Fe 2p3
Fe 2p1
O 1s
C 1s
Zn 3s
Fe 3p
Counts/s (Residualsx2)
50000
40000
30000
20000
10000
0
1000
800
600
400
200
0
Binding Energy (eV)

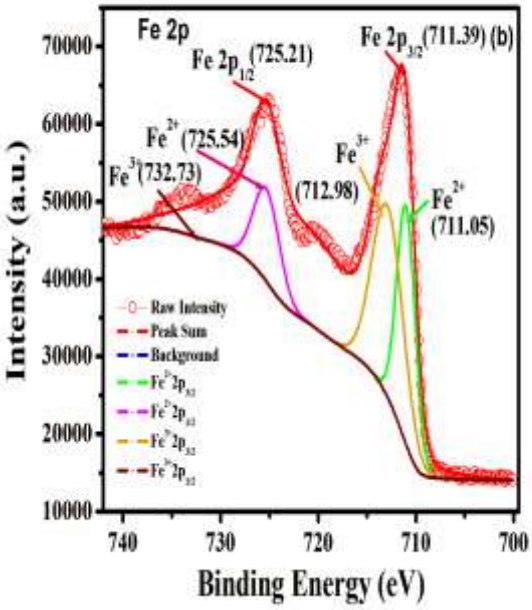
Fe 2p
Fe 2p1/2 (725.21)
Fe 2p3/2 (711.39) (b)
Fe2+ (725.54)
Fe3+ (732.73)
Fe3+ (712.98)
Fe2+ (711.05)
Raw Intensity
Peak Sum
Background
Intensity (a.u.)
Binding Energy (eV)

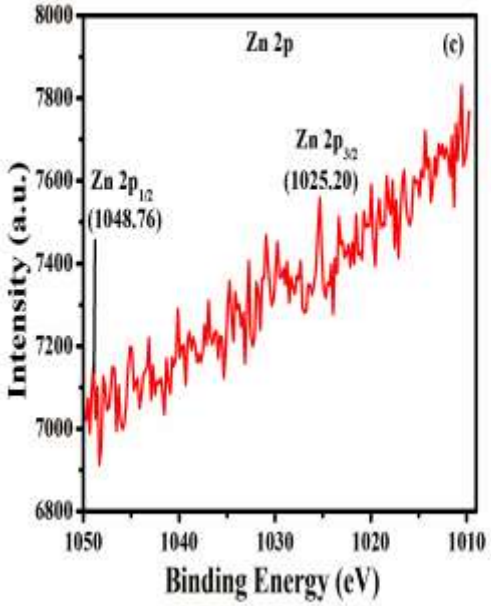
Zn 2p
(c)
Zn 2p1/2 (1048.76)
Zn 2p3/2 (1025.20)
Intensity (a.u.)
Binding Energy (eV)

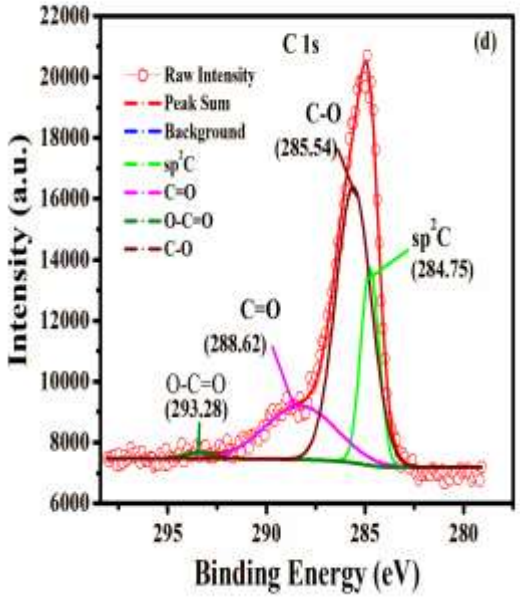

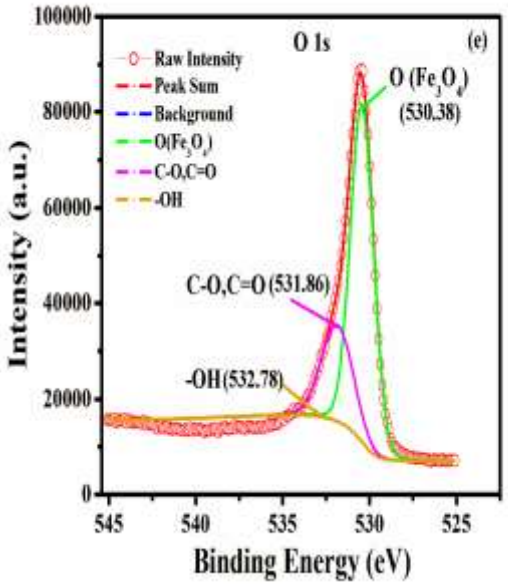

Fig.3 Synthesised G/Zn/F-NC XPS spectra: (a) The survey spectrum, (b) the Fe 2p, (c) Bi 2p, (d) C 1s and (e) O 1s spectra

3.2 Optical studies

Their UV-vis absorption spectra and band gap energy map were generated in order to evaluate the optical absorption and band gap characteristics of F-NPs, G/F-NCs, Zn/F-NPs and G/Zn/F-NCs. Optical absorption was seen at wavelengths of 404, 408, 414, and 411 nm for F-NPs, G/F-NCs, Zn/F-NPs and G/Zn/F-NCs, respectively. Fig.4(b) shows optical band gaps for F-

NPs, G/F-NCs, Zn/F-NPs and G/Zn/F-NCs of 2.97, 2.89, 2.68, and 2.77 eV, respectively. According to Cabot et al. (2007), bulk Fe_3O_4 has a band gap of 0.1 eV, which is less than that of the nanocomposites that have been created. The bandgap is widened by the inclusion of Zn and G dopants. The bandgap energies of Zn-doped Fe_3O_4 nanoparticles and undoped Fe_3O_4 nanoparticles, according to Anjana et al. (2018), were 2.4 and 2.25 eV, respectively. The bandgap energies of the cobalt codoped Fe_3O_4 nanoparticles and rGO were 1.901 eV, according to Anjana et al. (2023). The rGO and nickel-coated Fe_3O_4 nanoparticles, also known as Fe_3O_4, $Ni@Fe_3O_4$, $G@Fe_3O_4$, and $Ni/G@Fe_3O_4$ (Sherin et al.,2023), had optical bandgaps of 1.970 eV, 1.824 eV, 2.094 eV, and 2.130 eV, respectively. It is common established that as particle size decreases, a substance's band gap energy increases (Ferraz et al., 2021;Manikandan et al., 2014). A bandgap energy fell as the particle size rose, and the optical absorption in the current instance (Zn doping) was red shifted. This could be explained by differences in Zn and Fe's electronegativity and ionic radius caused by the formation of new defects structured as Fe atoms for Zn atoms. The system's higher disorder may be caused by the Zn 2p ions' larger ionic radius when compared to the Fe_2 ions, a basic metal. The bandgap energy reduction might be brought on by this. According to Modwi et al. (2019), the bandgap reduction and absorption redshift are most likely caused by the sp-d spin-exchange interactions between the band electrons and localised d-electrons in the Zn dopants. If the acceptor energy level drops below the conduction band or the donor energy exceeds the initial valence band, a decline will occur (Zhang et al., 2020). Additionally impure energy may be produced by Zn in the prohibited band. The above quantum confinement property of G/Zn/F-NCs is demonstrated by the high bandgap energy produced by the codoping of Zn and G into Fe_3O_4. The codopants absorbed smaller G/Zn/F-NCs more readily, which led to photocatalysis.

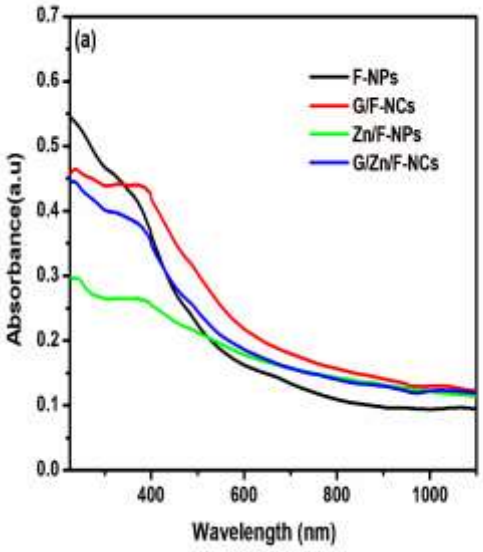

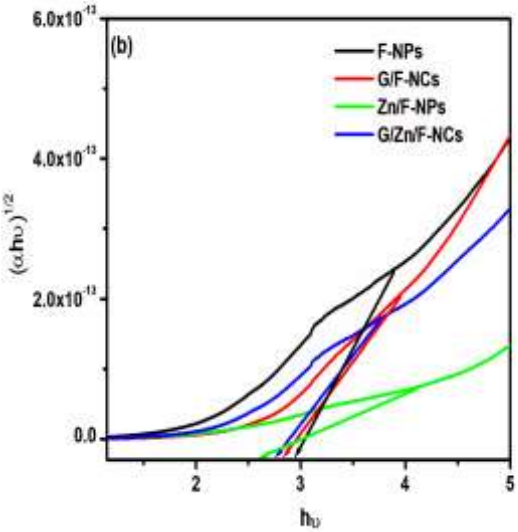

Figure 4(a) UV-visible spectra and (b) band gaps of F-NPs, G/F-NCs, Zn/F-NPs and G/Zn/F-NCs

Using photoluminescence (PL) spectroscopy, the produced nanoparticles' optical characteristics are further examined. As can be seen in Fig. 4(c), the absorption of F-NPs, G/F-NCs, Zn/F-NPs and G/Zn/F-NCs triggered at 340 nm all exhibit PL from the visible to near infrared region, but with varying intensities and wavelengths. Peaks of the absorption for F-NPs may be found at 359.91, 492.05, 519.87, and 593.63 nm. G/F-NC absorption peaks were measured at 362.06, 493.44, 521.24, and 592.85 nm. At 361.35, 494.61, 535.43, and 596.26 nm, Zn/F-NPs' absorption peaks can be seen. At wavelengths 361.35, 495.37, 535.42, and 596.26 nm, G/Zn/F-NCs exhibit their absorption peaks. Bulk Fe_3O_4, on the other hand, shows no PL. This results from the various particle confinement and spatial arrangements. Here, the contacts between the nanoparticles' surfaces are explained by high surface area (SA) per unit mass of the nanoparticle, which increases surface activity and has a propensity to react with the water molecules that are adsorbed during the chemical reaction. While in the Fe_3O_4, Fe^{2+} ions have a great affinity for interacting with water's oxygen molecules. When light strikes semiconductor materials, electrons and holes are produced. Fluorescence will be produced when holes and electrons unite again. To determine the separation rate of photoinduced charges, the PL characterizations of F-NPs, G/F-NCs, Zn/F-NPs and G/Zn/F-NCs were performed. The PL intensity of F-NPs was noticeably lower than that of G/Zn/F-NCs, as can be shown in Fig.4(c). In the F-NPs sample, the photogenerated charges' recombination efficiency was reduced because of the loaded Fe_3O_4 (Kexin et al., 2020). The luminescence exhibited on graphene and bismuth doped Fe_3O_4 is the result of charge transfer at the interface between the dopants and the oxide. Due to collective emissions and light scattering, dopants generate an excitonic emission peak that is conspicuous and red-shifted. According to Phan et al. (2011) and Fu et al. (2012), the chemical bonding of the dopants with Fe_3O_4 after the addition of graphene and zinc is what causes the higher absorbance and red shift of G/Zn/F-NCs in contrast to F-NPs.

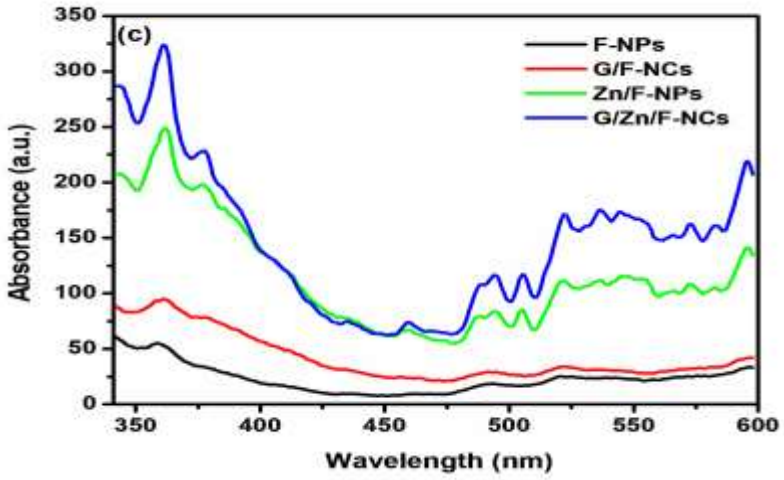

Fig.4(c) F-NP, G/F-NC, Zn/F-NP and G/Zn/F-NC PL absorption spectra

3.3 Vibrational Studies

Fig.5 shows the FTIR spectra of F-NPs, G/F-NCs, Zn/F-NPs, and G/Zn/F-NCs. Characteristic peaks were seen in the spectra around the wavelengths of 3453.12, 2936.24, 2841.68, 1627.07, 1378.39, 1163.22, 1037.95, 839.51, 538.64, and 459.23 cm^{-1}. According to Haw et al. (2011), the water molecules' O-H vibrations on the surface of the nanoparticles are responsible for the broad bands at 3453.12 cm^{-1}. According to Haw et al. (2011), the vibrations of C=O, C-C, and C-H stretching are represented by the bands at 1627.07, 1378.39cm^{-1}, and 800.57 cm^{-1}. G/Zn/F-NCs and G/F-NCs samples contain graphene, as evidenced by the presence of and C=O groups. And these diminished vibrations indicate that the presence of Fe^{3+} and Fe^{2+} ions from Fe_3O_4 weakens the vibrations of the carbon bonds (Rezapour et al., 2018; Lyubutin et al., 2018; Sharma et al., 2017). The nanocomposite's C-N stretching vibration is responsible for the peaks seen between 1262.43 and 924.11 cm^{-1} (Liu et al., 2018). The C-O stretching vibrations, which are seen in the graphene inclusion with Fe_3O_4 nanoparticle in the FTIR spectra of G/F-NCs correlate to a vibration signal at about 1135.78 cm^{-1}. The creation of the Fe_3O_4 spinel structure is confirmed by the bands at 763.31, 538.64, and 459.23 cm^{-1} in the Fe-O stretching vibrations of Fe^{2+} and Fe^{3+} ions at octahedral and tetrahedral positions in the FTIR spectra of F-NPs (Agnihotri et al., 2020; Keiser et al., 1982). The bands at 763.31, 538.64, and 459.23 cm^{-1} in The positions of the G/Zn/F-NCs' FTIR spectra have been changed towards 781.23, 545.52, and 469.47 cm^{-1}. The Fe^{2+} ions in the Fe_3O_4 lattice were thought to be the cause of the band shifting, which was related to the bond length replacement were switched out for Zn ions (Yang et al., 2009).A successful integration of zinc ions into the Fe_3O_4 lattice occurred in G/Zn/F-NCs, according to the FTIR results.

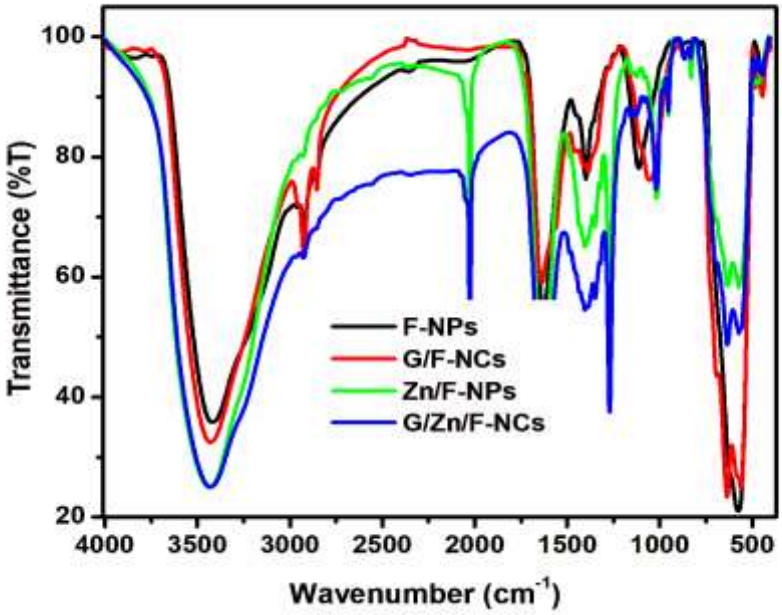

Figure 5 shows F-NPs, G/F-NCs, Zn/F-NPs and G/Zn/F-NCs FT-IR spectra

3.4 Morphological studies

The surface morphology of the synthesised F-NPs, G/F-NCs, Zn/F-NPs and G/Zn/F-NCs as observed by SEM examination is depicted in Fig. 6(a, b, c and d). The resultant nanoparticles are discovered to have a spherical form. Figure 6(e, f, g and h) shows the results of an analysis of the elemental makeup of the synthesised F-NPs, G/F-NCs, Zn/F-NPs, and G/Zn/F-NCs using EDAX measurement. There are iron signals in the EDAX spectra of each sample (F-NPs, G/F-NCs, Zn/F-NPs and G/Zn/F-NCs). It is confirmed that oxygen exists in the synthesised nanoparticles due to the presence of the oxygen signal at 0.5 keV. Large Fe and O peaks can be seen in the EDAX spectra, which is consistent with the synthesis of Fe_3O_4 nanoparticles. The carbon peak at 0.3 keV in the EDAX spectrum of the synthesised materials, G/Zn/F-NCs and G/F-NCs, indicates the presence of graphene. Zinc signals at 2.12 and 8.89 keV are visible in the G/Zn/F-NCs' EDAX spectra (Fig. 6(h)), supporting the presence of Zn in the Fe_3O_4 nanoparticles (Mishra et al., 2016). The elements' atomic percentages found by EDAX analysis are compiled in Table 2, Supporting Information.

(a) **(b)** **(c)** **(d)**

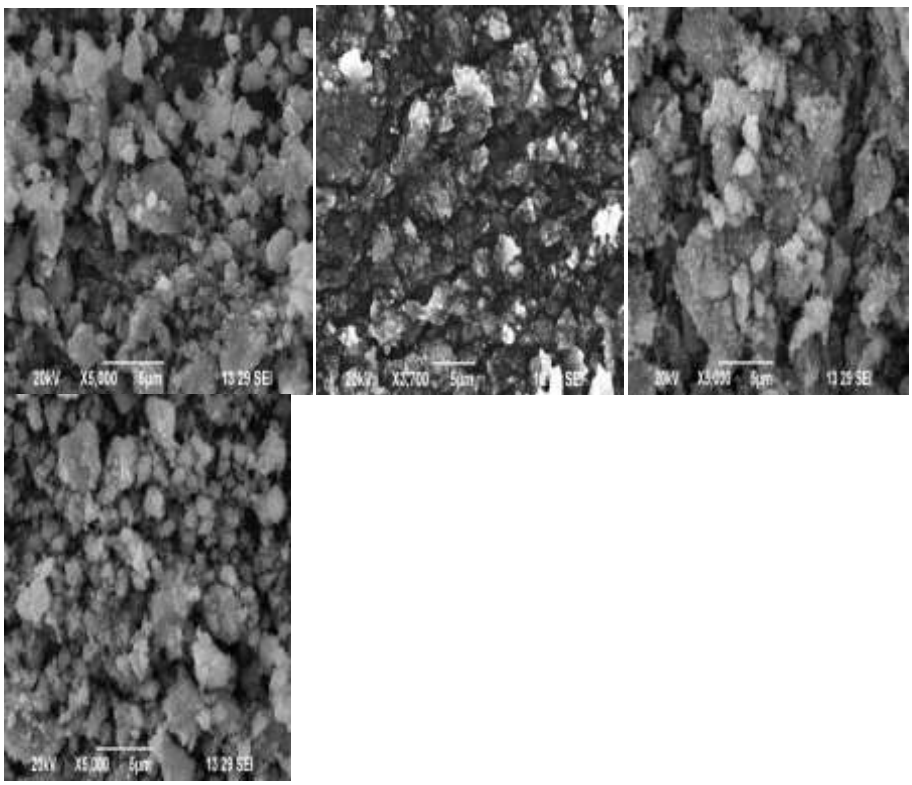

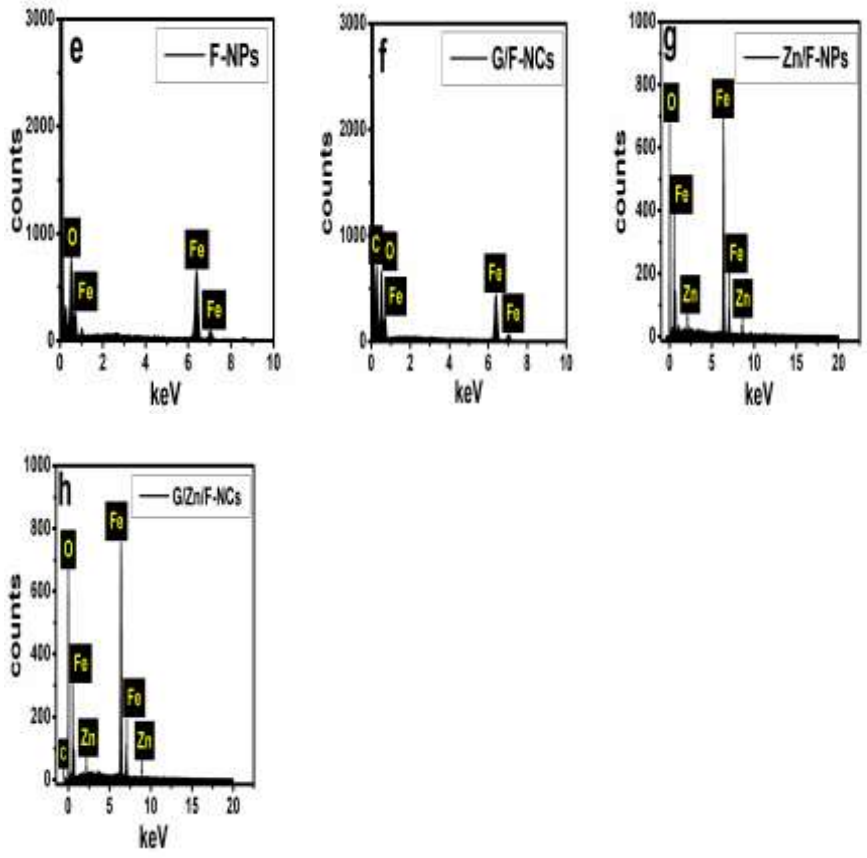
e
F-NPs
f
G/F-NCs
g
Zn/F-NPs
h
G/Zn/F-NCs
counts
keV
O
Fe
Zn
C

Fig.6 SEM images of (a) F-NPs, (b) G/F-NCs, (c) Zn/F-NPs and (d) G/Zn/F-NCs together with EDAX spectra of (e) F-NPs, (f) G/F-NCs, (g) Zn/F-NPs and (h) G/Zn/F-NCs

Table.2 Atomic percentage of elements detected by EDX analysis

Samples/Element	Fe		O		C		Zn	
	(wt.%)	(at.%)	(wt.%)	(at.%)	(wt.%)	(at.%)	(wt.%)	(at.%)
F-NPs	60.48	30.48	39.52	69.52	-	-	-	-
G/F-NCs	22.55	6.69	39.54	40.98	37.91	52.33	-	-
Zn/F-NPs	57.05	28.68	39.88	70.00			3.07	1.32
G/Zn/F-NCs	59.91	28.97	33.85	57.15	6.16	13.85	0.09	0.04

The microstructure of the samples of F-NPs, G/F-NCs, Zn/F-NPs and G/Zn/F-NCs that were studied using TEM analysis is shown in Fig.7(a, b, c and d). The produced Fe_3O_4 nanoparticles are confirmed to be crystalline in Fig.6. Fe_3O_4 nanoparticles may be seen scattered on the surface of graphene in the TEM images shown in Figure 7(b and d). F-NPs and Zn/F-NPs had average particle sizes determined at 35.72 and 42.03 nm, respectively. Additionally, the average particle sizes G/F-NCs and G/Zn/F-NCs for F-NPs were determined to be 39.14 and 41.18 nm, respectively. The aggregation of graphene during the chemical reaction is the cause of the slight rise in average particle size. This number is relatively close to the average crystal size estimated from XRD data. In iron oxide nanoparticles, C and Zn addition results in more uniform and spherical particle dispersion. SAED patterns for F-NPs, G/F-NCs, Zn/F-NPs, and G/Zn/F-NCs are depicted in Fig.7(e, f, g and h). Rings connected with the (111), (220), (311), (400), (422), (511) and (440) planes are seen in the SAED pattern for all F-NPs, G/F-NCs, Zn/F-NPs, and G/Zn/F-NCs. This is as a result of the creation of iron oxide nanoparticles. It has been demonstrated that all SAED patterns are highly intense, supporting the production of nanoparticles. In light of the lack of any other iron salts, the SAED pattern indicates the presence of Fe_3O_4 nanoparticles in their pure form (Sun et al., 2011).

(a) **(b)** **(c)** **(d)**

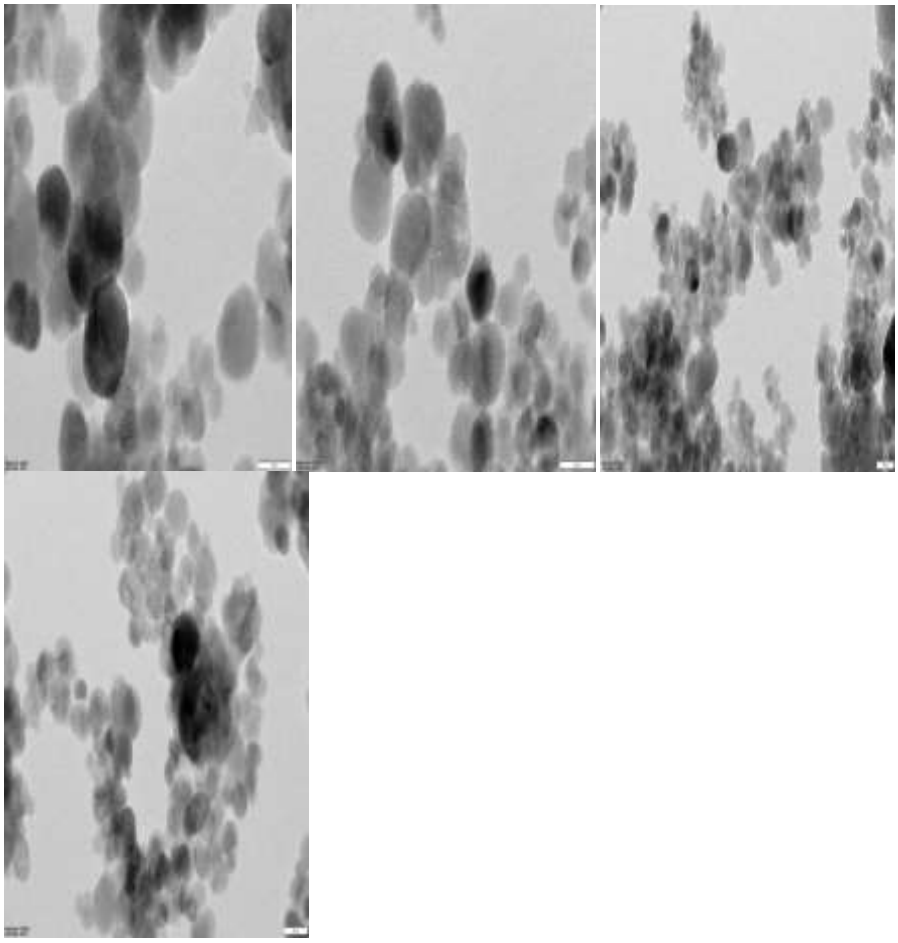

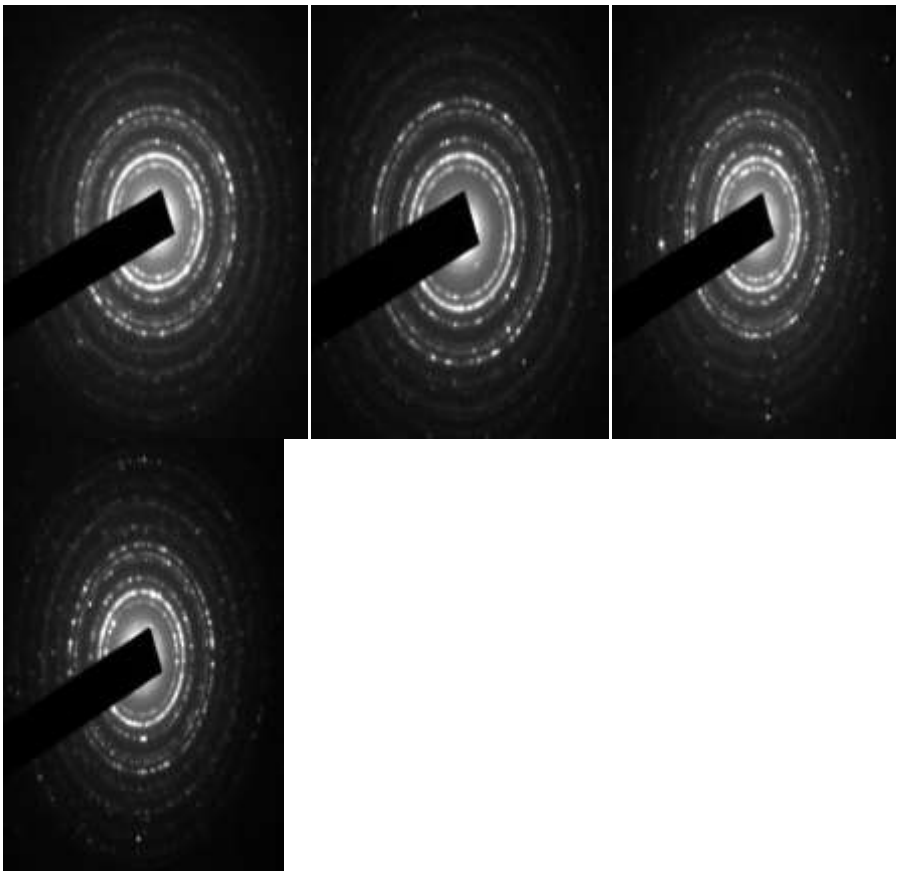

(e) **(f)** **(g)** **(h)**

Fig.7 shows TEM pictures and SAED patterns of F-NPs, G/F-NCs, Zn/F-NPs and G/Zn/F-NCs

3.5 BET surface area analysis

Fig.8 displays the samples' nitrogen-adsorption and -desorption isotherms with regard to F-NPs, G/F-NCs, Zn/F-NPs and G/Zn/F-NCs. Table 1 lists the prepared materials' surface areas, pore volumes, and pore diameters. At relative pressures between 0.4 and 1, the isotherms show prominent hysteresis loops, confirming the presence of mesoporous nanocomposites. The Brunauer-Emmett-Teller (BET) method is used to calculate, the surface areas of F-NPs, G/F-NCs, Zn/F-NPs and G/Zn/F-NCs were determined to be 48.742, 69.798, 49.514, and 71.115m^2/g, respectively. The increase in surface area of the samples after Zn and G doping is related to a reduction in the crystalline size of the Fe_3O_4 nanoparticles. A growth of secondary pores and the incorporation of graphene nanoflakes are responsible for the greater specific surface area of G/Zn/F-NCs (Su et al., 2011; Lian et al., 2010; Chen et al., 2011). Future studies on the adsorption of MB from wastewater will focus on the system with the highest G/Zn/F-NCs surface area because it is appropriate for adsorption applications (Aashima et al., 2019).

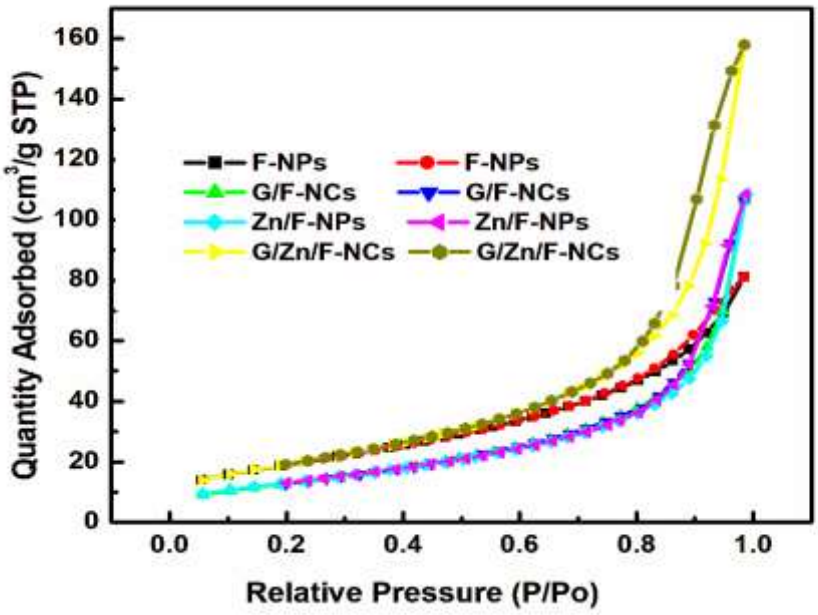

Figure 8 shows the isotherms for the adsorption and desorption of nitrogen on F-NPs, G/F-NCs, Zn/F-NPs and G/Zn/F-NCs

3.6 Antimicrobial activities of F-NPs, G/F-NCs, Zn/F-NPs and G/Zn/F-NCs

Staphylococcus aureus is efficiently contained medical implants despite the fact that it spreads and results in a number of harmful infections (Ribeiro et al., 2012). A common environmental bacterium called Pseudomonas aeruginosa infect people and cause a range of acute and chronic illnesses that might be fatal, especially individuals with compromised systemic defences (Qin et al., 2022). The spread of microorganisms with medication resistance is one of the main causes of the rise in death rates. Thus, it is highly recommended to find new approaches for developing pharmaceuticals that are efficient against certain bacterial strains. By employing the disc diffusion technique, it was determined whether F-NPs, G/F-NCs, Zn/F-NPs and G/Zn/F-NCs all demonstrated any antibacterial effects against a number of hazardous bacteria, including the often encountered water-borne gram-positive pathogen S. aureus and gram-negative pathogen P. aeruginosa, as well as fungi, Aspergillus flavus. (Fig.9 and dates are listed in Table 3). According to Fig. 9, the generated nanoparticles had a maximal zone of inhibition of 21 mm for S. aureus while ZOIs for A. flavus and P. aeruginosa were 16 and 18 mm, respectively.

Due to modifications in the structure of their cell walls, Staphylococcus aureus germs were discovered to be more vulnerable to chemical stressors than the other two species. When nanoparticles come into contact with S. aureus's cell membrane, it reacts, allowing more metal ions to get through. As a result, S. aureus suffers cell death and lessens its susceptibility to medication. The G/Zn/F-NCs nanocomposites show a significant antibacterial activity because of the dangers of toxicity, oxidative stress, and electron transport in graphene (Kumar et al., 2019). It can injure bacterial membranes directly by slicing into them with its pointed edges. By inactivating their lipids and proteins, bacteria can reproduce thanks to superoxide and hydroxyl radicals, singlet oxygen, and hydrogen peroxide are examples of reactive oxygen

species (ROS) that graphene can produce (Kumar et al., 2019). It functions as an electron acceptor and eliminates es from the membrane, possibly enhancing the membrane's integrity (Kumar et al., 2019). DNA deterioration, protein degradation, and lipid peroxidation are all outcomes of the Fenton reaction's production of ROS. Bacteria can be eliminated by ROS without hurting non-bacterial organisms. Both good and bad microbes were exposed to the bactericidal effects of ROS production. Kim et al. assert that Fe2 and oxygen combine to form hydrogen peroxide. The resultant hydrogen peroxide can harm biological molecules when it undergoes the Fenton reaction with ferrous ions(Kumar et al., 2019).

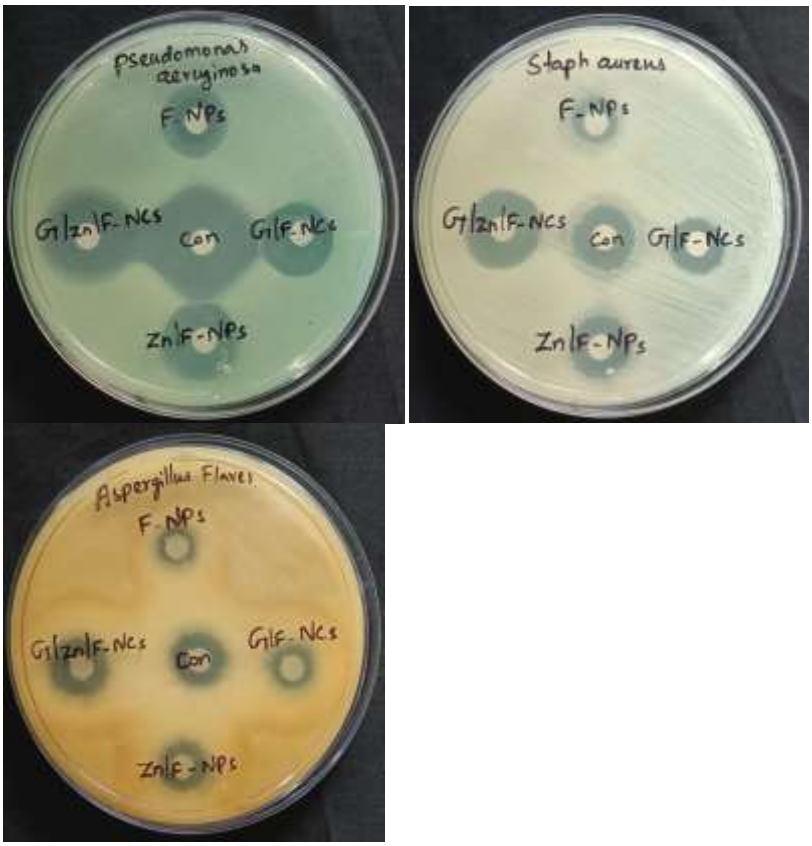

Figure 9 illustrates the ZOI of F-NPs, G/F-NCs, Zn/F-NPs and G/Zn/F-NCs for Pseudomonas aeruginosa, Staph aureus, and Aspergillus flaves

Table 3 ZOI of F-NPs, G/F-NCs, Zn/F-NPs and G/Zn/F-NCs

	F-NPs	G/F-NCs	Zn/F-NPs	G/Zn/F-NCs	Control (Amikacin)
Pseudomonas aeruginosa	15 mm	18 mm	19 mm	18mm	23 mm
Staph aureus	12 mm	14 mm	15 mm	21mm	16 mm

					Control (Nystatin)
Aspergillus Flaves	10 mm	12 mm	14 mm	16mm	15 mm

3.7 Photocatalytic degradation of F-NPs, G/F-NCs, Zn/F-NPs and G/Zn/F-NCs

Because it converts harmful contaminants into tiny, inorganic molecules (CO_2 and H_2O), photocatalytic degradation is one of the most essential and effective techniques to disinfect industrial waste water using light irradiation (Arefeh et al., 2019; Su shiung et al., 2020). Waste products from industrial dyeing are very hazardous, negatively affect the environment and are not biodegradable. Methylene blue (MB), a carcinogenic phenothiazine derivative used in the dyeing of textiles, is exceedingly dangerous and toxic. The photocatalytic degradation of aqueous MB under UV light in the presence of generated nanocatalysts (F-NPs, G/F-NCs, Zn/F-NPs and G/Zn/F-NCs) has been examined in this paper at various time intervals. As demonstrated in Fig. 10(a-d), MB was photocatalytically degraded across F-NPs, G/F-NCs, Zn/F-NPs and G/Zn/F-NCs. With 330 minutes of exposure, it demonstrated a stepwise decrease in the intensity of MB absorption at 661 nm, confirming that MB is degraded by clinging to the surface of the nanocatalysts that were created.

Photons can be effectively absorbed due to the great UV absorption of nanocomposite. From the electrons on the surface of Fe_3O_4 are transferred from the graphene valence to conduction band. These trapped electrons produce O_2 (super oxide radical), which promotes electron hole separation and they are trapped on the graphene surface. The recombination of electron-hole pairs in Fe_3O_4 was controlled by graphene's greater electronic conductivity, which started when sp^2 hybridization was restored and continued throughout the reduction process. According to Hisatomi et al. (2014) and Hoffmann et al. (1995), the redox interaction of the MB molecules with the catalyst is mediated by the electron-hole pairs. The Fe_3O_4's holes (photo produced) combine water, OH and MB dye to produce an active ingredient called a hydroxyl free radical. The ability of the conduction band to decrease molecular oxygen and the valence band to produce hydroxyl radicals are both favourable at the nanoparticles' surfaces. The organic dyes that are present on the surface of the G/Zn/F-NCs are affected by the hydroxyl radicals that are created because they act as oxidising agents.

$$Fe_3O_4 + H\nu \rightarrow h^+_{vb} + e^-_{cb}$$

$$(O_2)_{ads} + e^-_{cb} \rightarrow {}^{\cdot}O_2^-$$

$$H_2O + h^+ \rightarrow H^+ + OH^{\cdot}$$

Although the super oxide radicals still interact with H^+ to form HO_2 even if they are no longer involved in oxidation. As a result, when HO_2 and additional trapped e- at the valence band reacted with water/dyes, hydroxyl free radicals (active spices) were created. These radicals are created by the photocatalytic oxidation of water and reduction of oxygen on photocatalyst surfaces (Behnam et al., 2021).

$${}^{\cdot}H^+ + O_2^- \rightarrow HO_2^{\cdot}$$

$$e^- + HO_2^{\cdot} \rightarrow OH^{\cdot}$$

Therefore, the radicals O_2, HO_2, and OH_2 break down MB into its breakdown byproducts, such as CO_2 and H_2O.

$OH^{\cdot}$ / $HO_2^{\cdot}$ /O_2^{-} + MB → Degradation Products

Within 330 minutes of irradiation, it has been showed that F-NPs, G/F-NCs, Zn/F-NPs and G/Zn/F-NCs contribute 62%, 71%, 59%, and 94% to the corresponding degradation of MB contaminants. When compared to F-NPs, G/F-NCs and Zn/F-NPs, G/Zn/F-NCs have a higher degradation efficiency. The pseudo-first-order kinetic equation was used to compute the rate constant (k_{app}) of this catalytic process (Asha et al., 2021; Bessy et al., 2022; Ancy et al., 2021; Bindhu et al., 2021); the resulting linear plot of ln (A_t/A_0) and time is depicted in Fig. 10(e) below. Specifically, for F-NPs, G/F-NCs, Zn/F-NPs and G/Zn/F-NCs, k_{app} values of 0.005, 0.007, 0.003 and 0.009/min were given. G/Zn/F-NCs have a bigger predicted k_{app} value because of their high adsorption capacity (caused by the abundance of high light dispersion and additional active sites for the binding of MB molecules on their surfaces), which results in huge photoactivity. Due to graphene's high surface area and superior electrical conductivity, G/Zn/F-NCs can increase photocatalytic activity enhances the interaction of the dye molecules with the catalyst through electron transfer, hydroxyl radicals, and reactive sites. According to Hoffman et al. (1995), the thiazine ring in MB makes the photocatalyst more sensitive to light and makes it more vulnerable to photoreduction.

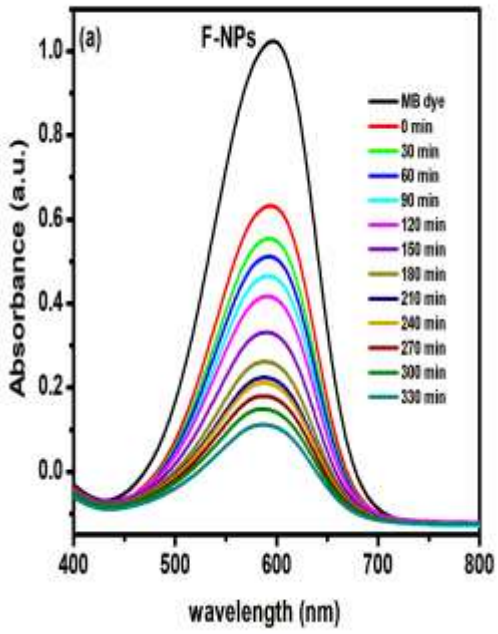

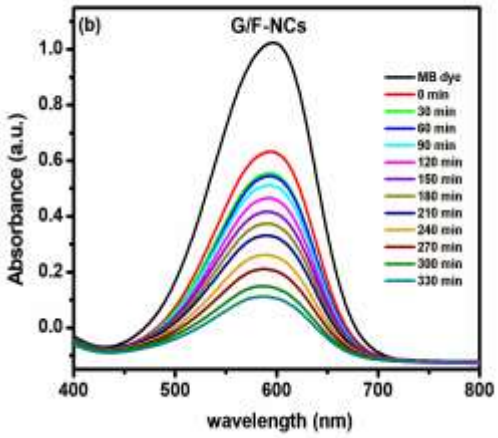
(b)
G/F-NCs
Absorbance (a.u.)
wavelength (nm)
MB dye
0 min
30 min
60 min
90 min
120 min
150 min
180 min
210 min
240 min
270 min
300 min
330 min

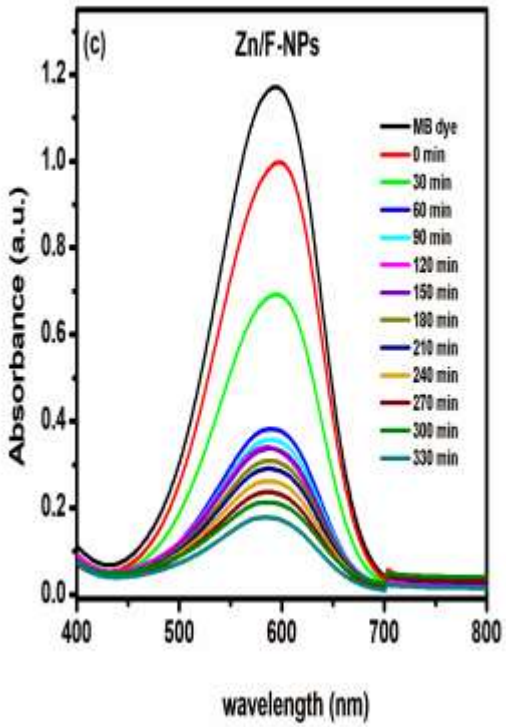
(c)
Zn/F-NPs
Absorbance (a.u.)
wavelength (nm)
MB dye
0 min
30 min
60 min
90 min
120 min
150 min
180 min
210 min
240 min
270 min
300 min
330 min

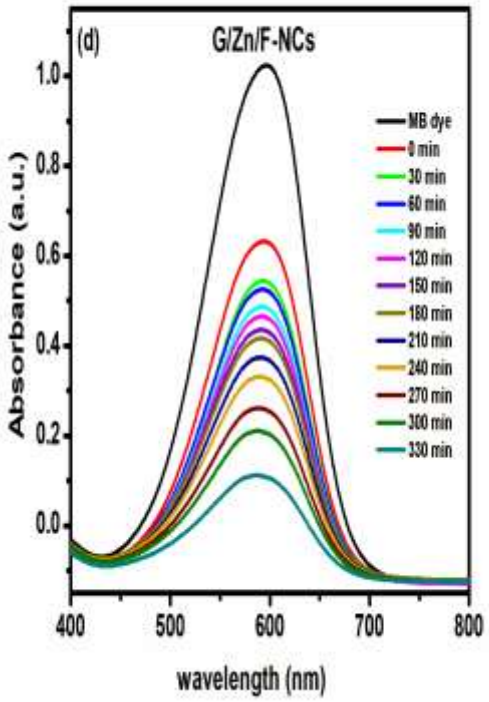
(d)
G/Zn/F-NCs
Absorbance (a.u.)
wavelength (nm)
MB dye
0 min
30 min
60 min
90 min
120 min
150 min
180 min
210 min
240 min
270 min
300 min
330 min

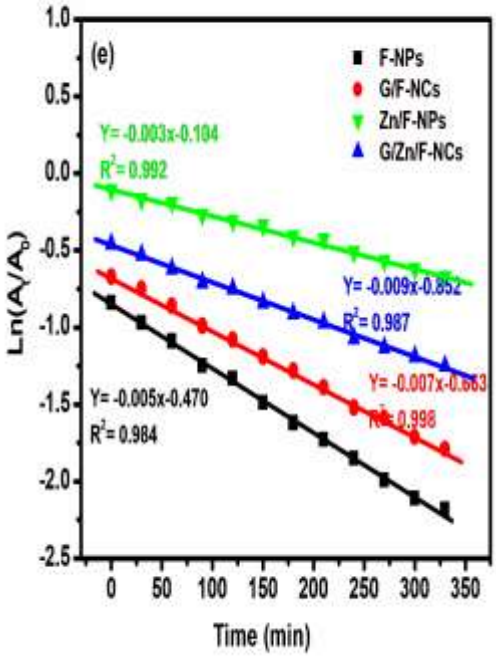
(e)
F-NPs
G/F-NCs
Zn/F-NPs
G/Zn/F-NCs
Y= -0.003x-0.104
R2= 0.992
Y= -0.009x-0.852
R2= 0.987
Y= -0.007x-0.663
R2= 0.998
Y= -0.005x-0.470
R2= 0.984
Ln(A/A0)
Time (min)

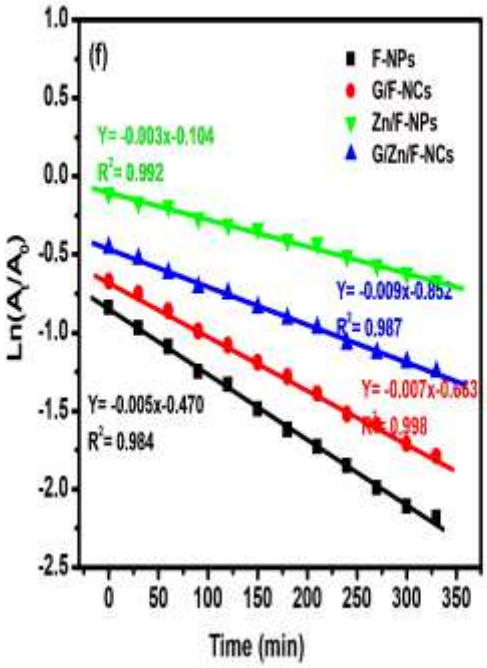

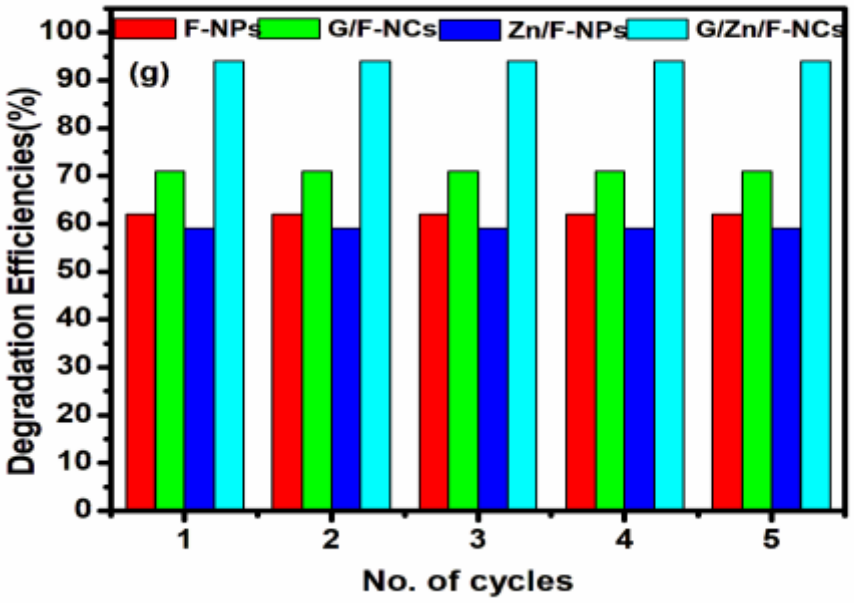

Figure 10 (a-d) shows the photocatalytic degradation curves for MB, (e) a linear plot of Ln (A_t/A_0) versus reaction time, (f) a linear plot of Ln (A_t/A_0) versus reaction time after seven days, and (g) a degradation (%) versus cycle count plot for F-NPs, G/F-NCs, Zn/F-NPs, and G/Zn/F-NCs.

The fact that there have been no appreciable changes to the rate constant values for F-NPs, G/F-NCs, Zn/F-NPs, and G/Zn/F-NCs even after seven days is evidence of their great stability towards the photocatalytic reaction (Fig.10(f)). Centrifugation is used to extract all of the produced photocatalysts from the reaction mixture. A total of five cycles of this experiment are performed using photocatalysts, with a similar 330-minute reaction period between cycles. The degradation efficiencies are seen to have not changed significantly (Fig. 10(g)). Because of this, the samples underwent 300°C calcination. The contaminants that may otherwise cause the photocatalyst to lose its activity may be removed by doing this. The stable catalytic activity F-NPs, G/F-NCs, Zn/F-NPs, and G/Zn/F-NCs) were therefore found, supporting their considerable reutilization for the degradation of MB. Fig. 11 shows a schematic representation of the process by which G/Zn/F-NCs degrade MB dye.

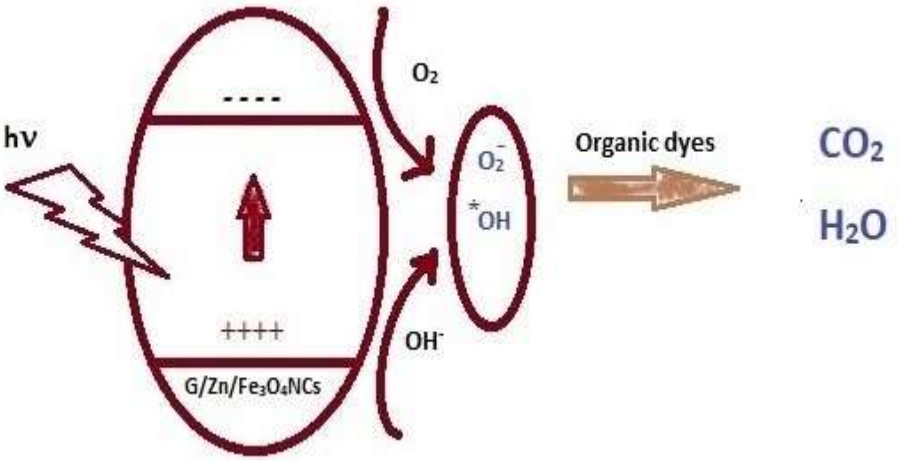

Fig.11 is a schematic representation of the process by which G/Zn/F-NCs degrade MB dye

4. Conclusion

The photocatalytic process and antibacterial properties with undoped, single- component doped and codoped nanocomposites of Fe_3O_4 (F-NPs, G/F-NCs, Zn/F-NPs and G/Zn/F-NCs) have been investigated to contrast the degradation of commercial colours. The fusion of G and Zn 2p ions into Fe_3O_4 was successfully demonstrated by the outcomes of XRD, XPS, FTIR, and EDAX. The approximate crystallite sizes were 34.22 nm, 38.61 nm, 41.58 nm, and 40.73 nm for F-NPs, G/F-NCs, Zn/F-NPs and G/Zn/F-NCs respectively, according to Scherrer's equation. F-NPs, G/F-NCs, Zn/F-NPs and G/Zn/F-NCs had optical bandgaps of 2.97, 2.89, 2.68, and 2.77 eV, respectively. F-NPs, G/F-NCs, Zn/F-NPs and G/Zn/F-NCs were found to have BET surface areas of 48.742, 69.798, 49.514, and 71.115m^2/g, respectively. The calculated k_{app} values were 0.005, 0.007, 0.003 and 0.009/min for F-NPs, G/F-NCs, Zn/F-NPs, and G/Zn/F-NCs, respectively. The expected k_{app} value was higher because G/Zn/F-NCs have a high capacity for light absorption and light diffusion due to their strong photoactivity. With respect to S. aureus, the produced nanoparticles had a maximal ZOI of 21 mm. The incorporation of double-dopants boosted the precise surface area and increased electron interaction between components towards enhance a composite's electrical conductivity, catalytic performance and antibacterial properties. We showed that nanocomposites containing zinc and graphene are probably going to improve the bacterial binding of nanoparticles.

5. List of abbreviations

Fe_3O_4	iron oxide nanoparticles
Zn	zinc
G	Graphene
F-NPs	nanoparticles of Fe_3O_4
G/F- NCs	Graphene-doped nanocomposites of Fe_3O_4
G/Zn/F-NCs	Iron oxide nanocomposites co-doped with zinc and graphene
XRD	X-ray diffraction
XPS	X-ray photoelectron spectroscopy
FTIR	Fourier transform - infra red spectroscopy
UV-vis	UV-visible spectroscopy
PL	Photoluminescence spectroscopy
TEM	Transmission electron microscopy
SEM	Scanning electron microscopy
EDAX	Energy dispersive
SAED	Selected area electron diffraction
BET	Brunauer Emmett Teller
ZOI	Zone of Inhibition
ROS	Reactive Oxygen Species
DNA	Deoxyribonucleic Acid
MB	Methylene blue
k_{app}	rate constant

References

1. Aashima, Shivani Uppal, Arushi Arora, Sanjeev Gautam, Suman Singh, R. J. Choudharyd and Mehta S. K. Magnetically retrievable Ce-doped Fe_3O_4 nanoparticles as scaffolds for the removal of azo dyes. RSC Adv., 2019, 9, 23129. DOI: 10.1039/c9ra03252e.
2. Aftabtalab, A and Sadabadi, H., "Application of magnetite (Fe_3O_4) nanoparticles in hexavalent chromium adsorption from aquatic solutions", Journal of Petroleum & Environmental Biotechnology, Vol. 6, No. 200, (2015), 1–6.
3. Agnihotri, P., Lad, V.N., 2020. Magnetic nanofluid: synthesis and characterization. Chem. Pap. 74, 3089–3100. https://doi.org/10.1007/s11696-020-01138-w.

4. Agusu, L., Alimin, Ahmad, L. O., Firihu, M. Z., Mitsudo, S., and Kikuchi, H. (2019). Crystal and Microstructure of $MnFe_2O_4$ Synthesized by Ceramic Method Using Manganese Ore and Iron Sand as Raw Material. Journal of Physics, 1-8.
5. Al-Farhan, B. S., "Removal of Cd and Pb Ions from Aqueous Solutions Using Bentonite-Modified Magnetic Nanoparticles", International Journal of Nano Dimension, Vol. 2, No. 1, (2016), 27–31.
6. Amara D., Felner I., Nowik I., Margel S., Synthesis and characterization of Fe and Fe_3O_4 nanoparticles by thermal decomposition of triiron dodecacarbony, Colloids Surf., A 339 (2009) 106-110.
7. Ancy, K., Vijilvani, C., Bindhu, M.R., Jeslin Sunitha Bai, S., Khalid, S.A., Turki, M.D., Ayman, M., Mohammed, S.A., 2021. Visible light assisted photocatalytic degradation of commercial dyes and waste water by Sn–F co-doped titanium dioxide nanoparticles with potential antimicrobial application. Chemosphere, 277, 130247. https://doi.org/10.1016/j.chemosphere.2021.130247.
8. Anjana P. M., Joe Sherin J. F., Vijayakumar C., Sarath Kumar S. R., Bindhu M. R., Rakhi R. B., Mater. Sci. Eng. B 2023, 290, 116313.
9. Anjana, P.M., Bindhu, M.R., Umadevi, M., Rakhi, R.B., 2018. Antimicrobial, electrochemical and photo catalytic activities of Zn doped Fe_3O_4 nanoparticles. J. Mater. Sci. Mater. Elect. 29, 6040-6050. https://doi.org/10.1007/s10854-018- 8578-2.
10. Arakha, M., Pal, S., Samantarrai, D., Panigrahi, T.K., Mallick, B.C., Pramanik, K., Mallick, B.,Jha, S., 2015. Antimicrobial activity of iron oxide nanoparticle upon modulation of nanoparticle-bacteria interface. Sci. Rep. 5(1), 14813. https://doi.org/10.1038/srep14813.
11. Arefeh Ahadi, Hassan Alamgholiloo, Sadegh Rostamnia, Xiao Liu, Mohammadreza Shokouhimehr, Diego A. Alonso, Rafael Luque, Layer-Wise Titania Growth Within Dimeric Organic Functional Group Viologen Periodic Mesoporous Organosilica as Efficient Photocatalyst for Oxidative Formic Acid Decomposition. The European Soceity Journal for Catalysis, 2019. 11(19) p. 4803-4809. https://doi.org/10.1002/cctc.201900486.
12. Asha, S., Hentry, C., Bindhu, M.R., Al-Mohaimeed, A.M., AbdelGawwad, M.R., Elshikh, M.S., 2021. Improved photocatalytic activity for degradation of textile dyeing waste water and thiazine dyes using PbWO4 nanoparticles synthesized by coprecipitation method. Environ. Res.200,111721. https://doi.org/10.1016/j.envres.2021.111721.
13. Ashraf, M.; Shah, S.S.; Khan, I.; Aziz, M.A.; Ullah, N.; Khan, M.; Adil, S.F.; Liaqat, Z.; Usman, M.; Tremel, W.; et al. A HighPerformance Asymmetric Supercapacitor Based on Tungsten Oxide Nanoplates and Highly Reduced Graphene Oxide Electrodes. Chem. Eur. J. 2021, in press.
14. Athar, T., 2015. Smart precursors for smart nanoparticles. Emerging Nanotechnologies for Manufacturing (Second Edition). Micro and Nano Tech. 444-538. https://doi.org/10.1016/B978-0-323-28990-0.00017-8.
15. Bala, D. A., Ali, H., Eli, D and Yunana, T. "Optical Properties of Reduced Graphene Oxide on Iron Oxide Nanoparticles", Vol. 3 No. 2, June, 2019, pp 226-231.
16. Balamurugan, J.; Nguyen, T. T.; Aravindan, V.; Kim, N. H.; Lee, J., Flexible Solid-State Asymmetric Supercapacitors Based on Nitrogen-Doped Graphene Encapsulated Ternary Metal-Nitrides with Ultralong Cycle Life. Advanced Functional Materials 2018, 28. http://dx.doi.org/10.1002/adfm.201804663.
17. Balamurugan, J.; Nguyen, T. T.; Aravindan, V.; Kim, N. H.; Lee, S. H.; Lee, J. H., All ternary metal selenide nanostructures for high energy flexible charge storage devices. Nano Energy 2019, 65, 10 https://doi.org/10.1016/j.nanoen.2019.103999.
18. Balamurugan, J.; Thanh, T. D.; Kim, N. H.; Lee, J. H., Facile synthesis of 3D hierarchical Ndoped graphene nanosheet/cobalt encapsulated carbon nanotubes for high energy density asymmetric supercapacitors. Journal of Materials Chemistry A 2016, 4 (24), 9555-9565. https://doi.org/10.1039/C6TA03132C.
19. BehnamNayebi, Kasra Pourrostami Niavol, Behzad Nayebi, Soo Young Kim, Ki Tae Nam, Ho Won Jang, Rajender S. Varma and Mohammadreza Shokouhimehr, Prussian blue-based nanostructured materials: Catalytic applications for environmental remediation and energy conversion. Molecular Catalysis, 2021. 514. p. 111835. https://doi.org/10.1016/j.mcat.2021.111835.

20. Beji, Z., Hanini, A., Smiri, L. S., Gavard, J., Kacem, K., Villain, F., et al. (2010). Magnetic properties of Zn-Substituted $MnFe_2O_4$ Nanoparticles Synthesized in Polyol as Potential Heating Agents for Hyperthermia. Evaluation of Their Toxicity on Endhothelial Cells. Chemistry of Materials, 5420-5429.
21. Bessy, T.C., Bindhu, M.R., Johnson, J., Chen, S.-M., Chen, T.-W., Almaary, K. S., 2022. UV light assisted photocatalytic degradation of textile waste water by Mg0.8- xZnxFe2O4 synthesized by combustion method and in-vitro antimicrobial activities. Environ. Res. 111917. https://doi.org/10.1016/j.envres.2021.111917.
22. Bharath, G.; Hai, A.; Kiruthiga, T.; Rambabu, K.; Sabri, M. A.; Park, J.; Choi, M. Y.; Banat, F.; Haija, M. A., Fabrication of Ru–$CoFe_2O_4$/RGO hierarchical nanostructures for high-performance photoelectrodes to reduce hazards Cr(VI) into Cr(III) coupled with anodic oxidation of phenols. Chemosphere 2022, 13443. https://doi.org/10.1016/j.chemosphere.2022.134439.
23. Bindhu, M.R., Willington, T.D., Hatshan, M.R., Chen, S.-M., Chen, T.-W., 2021. Environmental photochemistry with Sn/F simultaneously doped TiO_2 nanoparticles: UV and visible light induced degradation of thiazine dye. Environ. Res. 112108. https://doi.org/10.1016/j.envres.2021.112108.
24. Cabot, A., Puntes, V. F., Shevchenko, E., Yin, Y., Balcells, L., Marcus, M. A., Hughes, S.M., Alivisatos, A.P., 2007. Vacancy Coalescence during Oxidation of Iron Nanoparticles. J. American Chem. Soc. 129(34), 10358-10360. http://doi.org/10.1021/ja072574a.
25. Cao, W., Ma, Y., Zhou, W and Guo, L., "One-pot hydrothermal synthesis of
26. Chandra, V., Park, J., Chun, Y., Lee, J.W., Hwang, I.C., Kim, K.S., 2010. Waterdispersible magnetite- reduced graphene oxide composites for arsenic removal. ACS Nano 4, 3979e3986. http://dx.doi.org/10.1021/nn1008897.
27. Chang Y. C and Chen D. H., J. Colloid Interface Sci., 283, 446-451 (2005).
28. Chang, Y., Li, J., Wang, B., Luo, H., He, H., Song, Q., Zhi, L., 2013. Synthesis of 3D nitrogen-doped graphene/Fe_3O_4 by a metal ion induced self-assembly process for high-performance Li-ion batteries. J. Mater. Chem. A, 1(46), 14658-14665. http://doi.org/10.1039/c3ta13370b.
29. Chen D. Y., Ji G., Ma Y., Lee J. Y., Lu J. M., ACS Appl. Mater. Interfaces 2011, 3, 3078.
30. Chen H. I and Chang H. Y: Colloid Surface A, 2005, 242, 61-69.
31. Chen, R., Chen, R., Chai, L., Li, Q., Shi, Y., Wang, Y., Mohammad, A., 2013. Preparation and characterization of magnetic Fe_3O_4/CNT nanoparticles by RPO method to enhance the efficient removal of Cr(VI). Environ. Sci. Pollut. Res. Int. 20(10), 7175-85. http://doi.org/10.1007/s11356-013-1671-4.
32. Chen, Y., Fu, X.-Y., Yue, Y.-Y., Zhang, N., Feng, J., Sun, H.-B., 2019. Flexible and transparent supercapacitor based on ultrathin Au/graphene composite electrodes. Applied Surface Sci. 467-468 104-111. http://doi.org/:10.1016/j.apsusc.2018.10.093.
33. Cheng Q. D., Gong S., Zhang Q., Wang R., Jiang L., J. Mater. Chem. A 2017, 5, 16386.
34. Chimezie, A.B., Hajian, R., Yusof, N.A., Woi, P.M. and Shams, N., "Fabrication of reduced graphene oxide-magnetic nanocomposite (rGO-Fe_3O_4) as an electrochemical sensor for trace determination of As (III) in water resources", Journal of Electroanalytical Chemistry, Vol. 796, (2017), 33–42.
35. Chin, A.B., Yaacob, I.I., 2007. Synthesis and characterization of magnetic iron oxide nanoparticles via w/o microemulsion and Massart's procedure. J. Mater. Processing Tech. 191(1), 235-237. https://doi.org/10.1016/j.jmatprotec.2007.03.011.
36. Chou, C. Y.; Kuo, P.C.; Yao, Y.D.; Sun, A. C.; Fang, Y.H.; Chen, S. C.; Huang, C. H.; Chen, J. W. Effects of Sintering Temperature on the Magnetoresistance and Microstructure of the Mixture of Fe_3O_4 and Cu-Ferrite Powder. IEEE Trans. Magn. 2005, 41, 2757-2759.
37. Cruz, I. F., Freire, C., Araújo, J. P., Pereira, C., Pereira, A. M., 2018. Multifunctional Ferrite Nanoparticles: From Current Trends Toward the Future. Magnetic Nanostructured Mater. 59-116. http://doi.org/10.1016/b978-0-12-813904-2.00003-6.
38. Cui, H., Yang, W., Li, X., Zhao, H and Yuan, Z., "An electrochemical sensor based on a magnetic Fe 3 O 4 nanoparticles and gold nanoparticles modified electrode for sensitive determination of trace amounts of arsenic (III)", Analytical Methods, Vol. 4, No. 12, (2012), 4176–4181.

39. Cunqing Ma, Kaiyu yang, Lili Wang, Xin Wang. Facile synthesis of reduced graphene oxide/Fe_3O_4 nanocomposite film. J Appl Biomater Funct Mater 2017; 15(Suppl 1):S1-S6. DOI: 10.5301/jabfm.5000341.
40. Deng H., Li X. L., Peng Q., Wang X., Chen J. P., Li Y. D., Monodisperse magnetic single-crystal ferrite microspheres, Angew. Chem. Int. Ed. 44 (2005) 2782-2785.
41. Dubus S., Gravel J. F., Drogoff B. L., Nobert P., Veres T and Boudreau D., Anal. Chem., 78, 4457-4464 (2006).
42. Farimani, M.H.R.; Shahtahmasebi, N.; Roknabadi, M.R.; Ghows, N.; Kazemi, A. Study of structural and magnetic properties of superparamagnetic Fe_3O_4/SiO_2 core–shell nanocomposites synthesized with hydrophilic citrate-modified Fe_3O_4 seeds via a sol–gel approach. Phys. E Low Dimens. Syst. Nanostruct. 2013, 53, 207–216.
43. Ferraz I. S. B., Castro T. J., Mantilla J., Coaquira J. A. H., Garg V. K., Oliveira A. C., Franco Jr A., Morais P. C., da Silva S. W., J. Alloys Compd. 2021, 887, 161398.
44. Gade N.E., Dar R.M., Mishra O.P., Khan J.R., Kumar V and Patyal A.: Evaluation of dose-dependent cytotoxic effects of graphene oxide-iron oxide nanocomposite on caprine Wharton's jelly derived mesenchymal stem cells. J. Anim. Res. 5, 415 (2015).
45. Gautam, S., Shandilya, P., Priya, B., Singh, V. P., Raizada, P., Rai, R., et al. (2017). Superparamagnetic $MnFe_2O_4$ Dispersed over Graphitic Carbon Sand Composite and Bentonite as Magnetically Recoverable Photocatalyst for Antibiotic Mineralization. Seperation and Purification Technology, 498-511.
46. Geim A.K., Novoselov, K.S. 2007. The rise of graphene. Nature Mater.6, 183-191.
47. Giraldo, L., Erto, A and Moreno-Piraján, J. C., "Magnetite nanoparticles for removal of heavy metals from aqueous solutions: synthesis and characterization", Adsorption, Vol. 19, No. 2–4, (2013), 465–474.
48. Green wood, Norman N, Earnshaw, Alan. Chemistry of the Elements (2nd ed.). Butterworth-Heinemann.1997; ISBN 978-0-08-037941-8.
49. Gupta, S.S., Sreeprasad, T.S., Maliyekkal, S.M., Das, S.K., Pradeep, T., 2012. Graphene from sugar and its application in water purification. ACS Appl. Mater. Interfaces 4156e4163. http://dx.doi.org/10.1021/am300889u.
50. Gurunathan S., Woong Han J., Eppakayala V and Kim J.: Green synthesis of graphene and its cytotoxic effects in human breast cancer cells. Int. J. Nanomed. 8, 1015 (2013).
51. Han, Q., Wang, Z., Xia, J., Chen, S., Zhang, X., Ding, M., Talanta 2012, 101, 388–395.
52. Hastak V., Bandi S., Kashyap S., Singh S., Luqman S., Lodhe M., Peshwe D.R and Srivastav A.K.: Antioxidant efficacy of chitosan/ graphene functionalized superparamagnetic iron oxide nanoparticles. J. Mater. Sci.: Mater. Med. 29, 154 (2018).
53. Haw, C.Y., Chia, C.H., Zakaria, S., Mohamed, F., Radiman, S., Teh, C.H., Khiew P.S., Chiu W.S., Huang, N.M., 2011. Morphological studies of randomized dispersion magnetite nanoclusters coated with silica. Ceramint. 37(2), 451-464. http://doi.org/10.1016/j.ceramint.2010.09.010.
54. He, Z.; Koza, J. A.; Mu, G. J.; Miller, A. S.; Bohannan, E. w.; switzer, J. A. Electrodeposition of $Co_xFe_{3-x}O_4$ Epitaxial Films and Superlattices. Chem. Mater. 2013, 25, 223-232.
55. Hisatomi, T., Kubota, J., Domen, K., 2014. Recent advances in semiconductors for photocatalytic and photoelectrochemical water splitting. Chem. Soc. Rev. 43(22), 7520–7535. http://doi.org/10.1039/c3cs60378d.
56. Hoffmann, M.R., Martin, S.T., Choi, W., Bahnemann, D.W., 1995. Environmental Applications of Semiconductor Photocatalysis. Chem. Rev. 95(1), 69– 96. http://doi.org/10.1021/cr00033a004.
57. Hong R. Y., Pan T. T and Li H. Z., J. Magn. Magn. Mater., 303, 60-68 (2006).
58. Hosseini, S.H., Asadnia, A., 2013. Polyaniline/Fe_3O_4 coated on $MnFe_2O_4$ nanocomposite: Preparation, characterization, and applications in microwave absorption. J. Inter. Physical Sci. 8(22), 1209-1217. http://doi.org/10.5897/IJPS12.576.
59. Hu C. Q., Gao Z. H and Yang X. R., Chem. Phys. Lett., 429, 513-517 (2006).
60. Hu F. Q., Li Z., Tu C. F and Gao M. Y., J. Colloid Interface Sci., 311 (2007)469-474.

61. Jalil, Z., Rahwanto, A., Mustanir, Akhyar and Handoko, E. (2017). Magnetic Behaviour of Natural Magnetite (Fe_3O_4) Extracted from Beach Sand Obtained by Mechanical Alloying Method. AIP Conference Proceeding 1862 (pp. 030023-1-030023-4). Depok: AIP Publishing.
62. Jedrzejczak-Silicka M.: Cytotoxicity and genotoxicity of GO– Fe_3O_4 hybrid in cultured mammalian cells. Pol. J. Chem. Technol. 19, 27 (2017).
63. Joe Sherin J. F., Vijayakumar C., Bindhu M. R., Mansour K. Gatasheh, Ashraf Atef Hatamleh and Selvaraj Arokiyara, Phys. Status Solidi A 2023, 220, 2300076.
64. Jones H. The theory of the galvomagnetic effects in bismuth. Proceedings of the Royal Society of London. Series A: Mathematical and Physical Sciences. 1936;155(886):653-663. DOI: 10.1098/rspa.1936.0126.
65. Karim, M. R.; Mohammad, A.; Cho, M. H.; Yoon, T., Synergistic performance of Fe_3O_4/SnO_2/rGO nanocomposite for supercapacitor and visible light-responsive photocatalysis. International Journal of Energy Research 2022, 46 (5), 65 https://doi.org/10.1002/er.7588.
66. Keiser, J.T., Brown, C.W., Heidersbach, R.H., 1982. The Electrochemical Reduction of Rust Films on Weathering Steel Surfaces. J. Electrochem. Soc. 129(12), 2686. http://doi.org/10.1149/1.2123648.
67. Kexin Fang, Lei Shi, Lizhu Yao, Lishuang Cui. Synthesis of novel magnetically separable $Fe_3O_4/Bi_{12}O_{17}C_{l2}$ photocatalyst with boosted visible-light photocatalytic activity. 129(2020)110888.
68. Khaghani S, Ghanbari D, Khaghani S. Green synthesis of iron oxide-palladium nanocomposites by pepper extract and its application in removing of Colored pollutants from water. Journal of Nanostructures. 2017;7(3):175-182.
69. Kim E. H., Lee H. S., Kwak B. K and Kim B. K., J. Magn. Mater., 289, 328-330 (2005).
70. Kim, D. H., Nikles, D.E., and Brazel, C. S. (2010). Synthesis and Characterization of Multifunctional Chitosan-$MnFe_2O_4$ Nanoparticles for Magnetic Hyperthermia and Drug Delivery. Materials, 4051-4065.
71. Kumar P., Huo P., Zhang R., Liu B., Nanomaterials 2019, 9, 737
72. Lassoued A., Lassoued M. S., García-Granda S., Dkhil B., Ammar S., Gadri A., J. Mater. Sci. 2018, 29, 5726
73. Laurent S., Forge D., Port M., Roch A., Robic C., Vander Elst L., Muller R.N., Magnetic iron oxide nanoparticles: synthesis, stabilization, vectorization, physico-chemical characterizations, and biological applications, Chem. Rev. 108 (2008) 2064-2011.
74. Laurent, S.; Forge, D.; Port, M.; Roch, A.; Robic, C.; Elst, L. V.; Muller, R. N. Chem. Rev. 2008, 108, 2064.
75. Lazarevic, Z. Z., Jovalekic, C., Milutinovic, A., Sekulic, D., Ivanoski, V. N., and Recnik, A. (2013). Nanodimensional Spinel $NiFe_2O_4$ and $ZnFe_2O_4$ Ferrites Prepared by soft Mechanochemical Synthesis. Journal of Applied Physics, 1-11.
76. Lee J W, Kim J D. In Situ Chemical Synthesis of Fe_3O_4 Nanoparticles on Reduced Graphene Oxide Sheets in Polyol Medium and Magnetic Properties[J]. Journal of nanoscience and nanotechnology, 2015, 15/1: 215-219.
77. Li Y. X., Zhou X. Z., Wang Y and You X.Z.: Mater. Lett., 2004, 58, 245-249.
78. Li, X. F. et al. Synergistic effect of efficient adsorption g-C_3N_4/ZnO composite for photocatalytic property. J. Phys. Chem. Solids. 75, 441–446 (2014).
79. Lian P. C., Zhu X. F., Xiang H. F., Li Z., Yang W. S., Wang H. H., Electrochim. Acta 2010, 56, 834.
80. Liang JJ, Xu YF, Sui D, et al. Flexible, magnetic and electrically conductive graphene/Fe_3O_4 paper and its application for magnetic controlled switches. J Phys Chem C. 2010;114(41):17465-17471.
81. Liang, C., Song, J., Zhang, Y., Guo, Y., Deng, M., Gao, W., Zhang, J., 2020. Facile Approach to Prepare rGO@Fe_3O_4 Microspheres for the Magnetically Targeted and NIRresponsive Chemo-photothermal Combination Therapy. Nanoscale Res. Lett. 15(1), 86. http://doi.org/10.1186/s11671-020-03320-1.
82. Lin, L., Liu, Y., Zhao, X., Li, J. H., Anal. Chem. 2011, 83, 8396-8402.
83. Liu MM, Sun J. In situ growth of monodisperse Fe_3O_4 nanoparticles on graphene as flexible paper for supercapacitor. Journal of Materials Chemistry A. 2014;2(30):12068-12074.

84. Liu, L.; Zhu, X.; Zeng, Y.; Wang, H.; Lu, Y.; Zhang, J.; Yin, Z.-Z.; Chen, Z.; Yang, Y.; Li, L., An Electrochemical Sensor for Diphenylamine Detection Based on Reduced Graphene Oxide/Fe_3O_4-Molecularly Imprinted Polymer with 1,4-Butanediyl-3,3'- bis-l-vinylimidazolium Dihexafluorophosphate Ionic Liquid as Cross-Linker. Polymers 2018, 10, 13. http://dx.doi.org/10.3390/polym10121329.
85. Liu, S., Wang, Z. Y., Zhang, Y., Dong, Z & Zhang, T. Preparation of zinc oxide nanoparticle–reduced graphene oxide–gold nanoparticle hybrids for detection of NO_2. RSC Adv. 5, 91760–91765 (2015).
86. Liu, S.; Yu, B.; Wang, S.; Shen, Y.; Cong, H., Preparation, surface functionalization and application of Fe_3O_4 magnetic nanoparticles. Advances in Colloid and Interface Science 2020, 281, 10216. https://doi.org/10.1016/j.cis.2020.102165.
87. Liu, Y.; Wang, W.; Xu, X.; Marcel Veder, J.-P.; Shao, Z., Recent advances in anion-doped metal oxides for catalytic applications. Journal of Materials Chemistry A 2019, 7 (13), 7280-7300. https://doi.org/10.1039/C8TA09913H.
88. Lu, A.-H.; Salabas, E. L.; Schuth, F. Angew. Chem., Int. Ed. 2007, 46, 1222.
89. Lyubutin, I.S., Baskakov, A.O., Starchikov, S.S., Shih, K.-Y., Lin, C.-R., Tseng, Y.-T., Yang, S.-S., Han, Z.-Y., Ogarkova, Yu.L., Nikolaichik, V.I., Avilov, A.S., 2018. Synthesis and characterization of graphene modified by iron oxide nanoparticles. Mater. Chem. Phy. 219, 411-420. http://doi.org/10.1016/j.matchemphys.2018.08.042.
90. Mahalingam, S and Ahn, Y. H., "Improved visible light photocatalytic activity of rGO–Fe_3O_4–NiO hybrid nanocomposites synthesized by in situ facile method for industrial wastewater treatment applications", New Journal of Chemistry, Vol. 42, No. 6, (2018), 4372–4383.
91. Mahdavi M., Namvar F., Ahmad M. B and Mohamad R., Molecules, 18, 5954(2013) DOI: 10.3390/molecules 18055954.
92. Maity, D., Agrawal, D.C., 2007. Synthesis of iron oxide nanoparticles under oxidizing environment and their stabilization in aqueous and non-aqueous media. J. Magnetism and Magnetic Mater. 308(1), 46-55. http://doi.org/10.1016/j.jmmm.2006.05.001.
93. Mandal, P., Chattopadhyay, A.P., 2015. Excellent catalytic activity of magnetically recoverable Fe_3O_4–graphene oxide nanocomposites prepared by a simple method. Dalton Trans. 44(25), 11444-11456. http://doi.org/10.1039/c5dt01260k.
94. Manikandan A., Vijaya J. J., Mary J. A., Kennedy L. J., Dinesh A., J. Ind. Eng. Chem. 2014, 20, 2077.
95. Mary Eagleson. Concise encyclopedia chemistry. Walter de Gruyter.1994; ISBN 3-11-011451-8.
96. Matijevic E., sapieszko R.S., Melville J.B., Ferric hydrous oxide sols I. Monodispersed basic iron(III) sulfate particles, J. Colloid Interface Sci. 50 (1975) 567-581.
97. Mishra, A., Mohanty, T., 2016. Structural and morphological study of magnetic Fe3O4/ reduced graphene oxide nanocomposites. Materials Today: Proceedings 3(6), 1576-1581. https://doi.org/10.1016/j.matpr.2016.04.045.
98. Modwi A., Khezami L., Taha, A. Bessadok, S. Mokraoui, J. Mater. Sci. Mater. Electron. 2019, 30, 14714.
99. Moradinasab, S and Behzad, M., "Removal of heavy metals from aqueous solution using Fe_3O_4 nanoparticles coated with Schiff base ligand", Desalination and Water Treatment, Vol. 57, No. 9, (2016), 4028–4036.
100. Moyer, J. A.; Vaz, C. A. F.; Negusse, E.; Arena, D. A.; Henrich, V. E. Controlling the Electronic Structure of Co_{1-x} $Fe_{2+x}O_4$ Thin Films through Iron Doping. Phys. Rev. B 2011, 83, 035121.
101. Mozaffari M, shatooti S, Jafarzadeh M, Niyaifar M, Aftabi A, Mohammadpour H & Amiri S. 2015. Synthesis of Zn^{2+} substituted maghemite nanoparticles and investigation of their structural and magnetic properties. J Magn Magn Mater 382: 366-375.
102. Mussa, Y.; Ahmed, F.; Arsalan, M.; Alsharaeh, E. Two dimensional (2D) reduced graphene oxide (RGO)/hexagonal boron nitride (h-BN) based nanocomposites as anodes for high temperature rechargeable lithium-ion batteries. Sci. Rep. 2020, 10(1), 1-13, https://doi.org/10.1038/s41598-020-58439-z.

103. Namvari, M and Namazi, H., "Clicking graphene oxide and Fe_3O_4 nanoparticles together: an efficient adsorbent to remove dyes from aqueous solutions", International Journal of Environmental Science and Technology, Vol. 11, No. 6, (2014), 1527–1536.
104. Naseri, M. G., Saion, E. B., Ahangar, H. A., Hashim, M., and Shaari, A. H. (2011). Synthesis and Characterization of Manganese Ferrite Nanoparticles by Thermal Treatment Method. Journal of Magnetism and Magnetic Material, 1745- 1749.
105. Nayamadi Mahmoodabadi A., Kompany A., Mashreghi M., Mater. Chem. Phys. 2018, 213, 285.
106. Ng, W.C., Tan C.Y., Ong, B.H., Matsuda, A. Procedia Eng., 2017, 184, 587-594.
107. Novoselov K. S., Geim A. K., Morozov S. V., Jiang D., Zhang Y., Dubonos S. V., Grigorieva I. V., Firsov A. A., Science 2004, 306, 666.
108. Ou J, Wang F, Huang Y, et al. Fabrication and cyto-compatibility of Fe_3O_4/SiO_2/graphene-CdTe QDs/CS nanocomposites for drug delivery. Colloids Surf B Biointerfaces. 2014;117:466-472.
109. Padhi, D.K., Panigrahi, T.K., Parida, K., Singh, S.K and Mishra, P. M., "Green synthesis of Fe_3O_4/RGO nanocomposite with enhanced photocatalytic performance for Cr (VI) reduction, phenol degradation, and antibacterial activity", ACS Sustainable Chemistry & Engineering, Vol. 5, No. 11, (2017), 10551–10562.
110. Peik-See, T., Pandikumar, A., Ngee, L.H., Ming, H.N and Hua, C. C., "Magnetically separable reduced graphene oxide/iron oxide nanocomposite materials for environmental remediation", Catalysis Science & Technology, Vol. 4, No. 12, (2014), 4396– 4405.
111. Pelin M., Fusco L., León V., Martín C., Criado A., Sosa S., Vázquez E., Tubaro A and Prato M.: Differential cytotoxic effects of graphene and graphene oxide on skin keratinocytes. Sci. Rep. 7, 1 (2017).
112. Penc B., Hofmann M., Slaski M., Starowicz P and Szytula A.: J. Alloy. Compd. 1999, 282, 8-13.
113. Perreault F., De Faria A.F., Nejati S and Elimelech M.: Antimicrobial properties of graphene oxide nanosheets: Why size matters. ACS Nano 9, 7226 (2015).
114. Pistofidis N, Vourlias G, Konidaris S, Pavlidou E, Stergiou A, Stergioudis G. The effect of bismuth on the structure of zinc hot-dip galvanized coatings. Materials Letters. 2007; 61(4):994-997. DOI: 10.1016/j.matlet.2006.06.029.
115. Qiao, R; Yang, C.; Gao, M. J. Mater, Chem. 2009, 19, 6274.
116. Qin S., Xiao W., Zhou C., Pu Q., Deng X., Lan L., Liang H., Song X., Wu M., Signal Trans. Target Ther. 2022, 7, 199.
117. Ramanathan, S.; SasiKumar, M.; Radhika, N.; Obadiah, A.; Durairaj, A.; Helen Swetha, G.; Santhoshkumar, P.; Sharmila Lydia, I.; Vasanthkumar, S., Musa paradisiaca reduced graphene oxide (BRGO) /MWCNT-Fe_3O_4 nanocomposite for supercapacitor and photocatalytic applications. Materials Today: Proceedings 2021, 47, 843-85. https://doi.org/10.1016/j.matpr.2021.01.706.
118. Ramesh N., Ranganayakulu S.V. Size Dependent Optical and Magnetic Properties Of Zn Doped Iron Oxide Nanoparticles. Journal of Ovonic Research. Vol. 15, No. 2, March - April 2019, p. 135 – 141.
119. Rezapour, M., 2018. One-step electrochemical synthesis and characterization of high performance magnetite/reduced graphene oxide nanocomposite. Anal. Bioanal. Electrochem. 10, 450-464.
rGO-Fe_3O_4 hybrid nanocomposite for removal of Pb (II) via magnetic separation", Chemical Research in Chinese Universities, Vol. 31, No. 4, (2015), 508–513.
120. Riana, M., Sembiring, T., Situmorang, M. Kurniawan, C., Setiadi, E. A., Tetuko, A. P., et al. (2018). Preparation and Characterization of Natural Iron Sand from Kata Beach, Sumatera Barat Indonesia with High Energy Milling (HEM). Jurnal Natural, 97-100.
121. Ribeiro M., Monteiro F. J., Ferraz M. P., Biomatter 2012, 2, 176.
122. Santos C.M., Mangadlao J., Ahmed F., Leon A., Advincula R.C and Rodrigues D.F.: Graphene nanocomposite for biomedical applications: Fabrication, antimicrobial and cytotoxic investigations. Nanotechnology 23, 395101 (2012).
123. Setiadi, E. A., Yunus, M., Nababan, N., Simbolon, S., Kurniawan, C., Humaidi, S., et al. (2017). The Effect of Temperature on Synthesis of $MgFe_2O_4$ Based on Natural Iron Sand by Co-

precipitation Method as Adsorbent Pb Ion. Journal of Physics: Conference Series, Vol. 985, pp.012046.

124. Sharma, N., Sharma, V., Jain, Y., Kumari, M., Gupta, R., Sharma, S. K., Sachdev, K., 2017. Synthesis and Characterization of Graphene Oxide (GO) and Reduced Graphene Oxide (rGO) for Gas Sensing Application. Macromol. Symp. 376(1), 1700006. http://doi.org/10.1002/masy.201700006.
125. Sharma, N; Sharma, V; Sharma, S.K; Sachdev, K. Synthesis and Characterization of Graphene Oxide (GO) and Reduced Graphene Oxide (rGO) for Gas Sensing Application. Macromol. Symp. 2017, 376, 1700006. DOI: 10.1002/masy.201700006.
126. Simeonidis K., Mourdikoudis S., Moulla M., et al., J. Magnetism and Magnetic Materials., 316(2), e1(2007), DOI: 10.1016/j.jmmm.2008.01.028.
127. Somvanshi, S.B., Khedkar, M.V., Kharat, P.B., Jadhav, K.M., 2020. Influential diamagnetic magnesium (Mg2+) ion substitution in nano-spinel zinc ferrite ($ZnFe_2O_4$): Thermal, structural, spectral, optical and physisorption analysis. Ceramint. 46(7), 8640-8650. http://doi.org/10.1016/j.ceramint.2019.12.097.
128. Su shiung Lam, Van-Huy Nguyen, Minh Tuan Nguyen Dinh, Dinh Quang Khieu, Duc Duong La, Huu Trung Nguyen, Dai Viet N. Vo, Changlei Xia, Rajender S. Varma, Mohammadreza, Shokouhimehr, Chinh Chien Nguyen, Quyet Van Le and Wanxi Peng, Mainstream avenues for boosting graphitic carbon nitride efficiency: towards enhanced solar light-driven photocatalytic hydrogen production and environmental remediation. Journal of Materials Chemistry A, 2020. 8(21) p. 10571-10603. https://doi.org/10.1039/D0TA02582H.
129. Sun, J., Zhou, S., Hou, P., Yang, Y., Weng, J., Li, X., Li, M., 2006. Synthesis and characterization of biocompatible Fe_3O_4 nanoparticles. J. Biomed. Mater. Res. A, 80(2), 333-41. http://doi.org/10.1002/jbm.a.30909.
130. Sun, X.J., Liu, F.T., Jiang, Q.H., 2011. Synthesis and Characterization of Co^{2+} -Doped Fe_3O_4 Nanoparticles by the Solvothermal Method. Mater. Sci. Forum 688, 364-369. http://doi.org/10.4028/www.scientific.net/msf.688.364.
131. Sun, Y.F., Chen, W.K., Li, W.J., Jiang, T.J., Liu, J.H. and Liu, Z. G., "Selective detection toward Cd2+ using Fe_3O_4/RGO nanoparticle modified glassy carbon electrode", Journal of Electroanalytical Chemistry, Vol. 714, (2014), 97–102.
132. Takaobushi, J.; et al. Electronic Structures of $Fe_{(3-x)}M_{(x)}O_{(4)}$ (M=Mn, Zn) Spinel Oxide Thin Films Investigated by X-Ray Photo emission Spectroscopy and X-Ray Magnetic Circular Dichroism. Phys. Rev. B 2007, 76, 205108.
133. Tang N.J., Zhong W., Jiang H.Y., Nanostructured magnetite (Fe_3O_4) thin films prepared by sol-gel method, J. Magn. Magn. Mater.282(2004) 92-95.
134. Tang, L. H., Wang, Y., Li, Y. M., Feng, H. B., Lu, J., Li, J. H., Adv. Funct. Mater. 2009, 19, 2782–2789.
135. Tripathy, D.; Adeyeye, A. O. ; Boothroyd, C. B.; Piramanayagam, S. N. Magnetic and Transport Properties of Co-Doped Fe_3O_4 Films. J. Appl. Phys. 2007, 101, 013904.
136. Tsai M. S.: Mat. Sci. Eng. B, 2004, 110, 132-134.
137. Van-HuyNguyen, Ba-Son Nguyen, Zhong Jin, Mohammadreza, Shokouhimehr, Ho Won Jang, Chechia Hu, Pardeep Singh, Pankaj Raizada, Wanxi Peng, Su Shiung Lam, Changlei Xia, Chinh Chien Nguyen, Soo Young Kim and Quyet Van Le, Towards artificial photosynthesis: Sustainable hydrogen utilization for photocatalytic reduction of CO_2 to high-value renewable fuels. Journal of Chemical Engineering, 2020. 402. p. 126184. https://doi.org/10.1016/j.cej.2020.126184.
138. Vermisoglou, E.C., Jakubec, P., Bakandritsos, A., Pykal, M., Talande, S., Kupka, V., Zboril, R., Otyepka, M. Chemical Tuning of Specific Capacitance in Functionalized Fluorographene. Chem. Matter., 2019, 31(13), 4698-4709.
139. Wang, H., Yuan, X., Wu, Y., Chen, X., Leng, L., Wang, H., Li, H. and Zeng, G., "Facile synthesis of polypyrrole decorated reduced graphene oxide–Fe_3O_4 magnetic composites and its application for the Cr (VI) removal", Chemical Engineering Journal, Vol. 262, (2015), 597–606.

140. Wang, J., Tang, B., Tsuzuki, T., Liu, Q., Hou, X. & Sun, L. 2012. Synthesis, characterization and adsorption properties of superparamagnetic polystyrene/Fe_3O_4/graphene oxide. Chem. Eng. J. 204, 258–263.
141. Wang, W.P., Yang, H., Xian, T., Jiang, J.L., 2012. XPS and Magnetic Properties of $CoFe_2O_4$ Nanoparticles Synthesized by a Polyacrylamide Gel Route. Mater.Trans. 53(9), 1586-1589. http://doi.org/10.2320/matertrans.m2012151.
142. Wang, X. L., Bai, H., Jia, Y. Y., Zhi, L. J., Qu, L. T., Xu, Y. X., Li, C., Shi, G. Q., RSC Adv. 2012, 2, 2154–2160.
143. Wang, X. L., Bai, H., Yao, Z. Y., Liu, A. R., Shi, G. Q., J. Mater. Chem. 2010, 20, 9032–9036.
144. Wang, Y., Li, Z. H., Hu, D. H., Lin, C. T., Li, J. H., Lin,Y. H., J. Am. Chem. Soc. 2010, 132, 9274-9276.
145. Wang, Y., Shao, Y. Y., Matson, D. W., Li, J. H., Lin, Y. H., ACS Nano 2010, 4, 1790–1798.
146. Wang, Z. H., Xia, J. F., Zhu, L. Y., Chen, X. Y., Zhang, F. F., Yao, S. Y., Li, Y. H., Xia Y. Z., Electroanalysis 2012, 23, 2463–2471.
147. Wang, Z. H., Xia, J. F., Zhu, L. Y., Zhang, F. F., Guo, X. M., Li, Y. H., Xia, Y. Z., Sens. Actuators B: Chem. 2012, 161, 131–136.
148. Wu Z. Y., Xu X. X., Hu B. C., Liang H. W., Lin Y., Chen L. F., Yu S. H., Angew. Chem. 2015, 54, 8179.
149. Wu, Q.; Xu, Y.; Yao, Z.; Liu, A.; Shi, G. Supercapacitors based on flexible graphene/polyaniline nanofiber composite films. ACS Nano 2010, 4, 1963–1970.
150. Xu Z. C., Shen C.M., Hou Y.L., Gao H.J., Sun S.H., Oleylamine as both reducing agent and stabilizer in a facile synthesis of magnetite nanoparticles, Chem. Mater.21 (2009) 1778-1780.
151. Yadav, R. S., Kuritka, I., Vilcakova, J., Masilko, J., Kalina, L., et al. (2017). Structural, Magnetic, Dielectric and Electric Properties ov $NiFe_2O_4$ Spinel Ferrite Nanoparticles Prepared by Honey- Mediated Sol-Gel Combustion. Journal of Physical and Chemistry of Solids, 1-42.
152. Yang W., Ratinac K. R., Ringer S. P., Thordarson P., Gooding J. J., Braet F., Angew. Chem. Int. Ed. 2010, 49, 2114.
153. Yang X., Zhang X., Ma Y., Huang Y., Wang Y., Chen Y., Superparamagnetic graphene oxide–Fe_3O_4nanoparticles hybrid for controlled targeted drug carriers, J. Mater. Chem. 19 (18) (2009) 2710–2714, https://doi.org/10.1039/b821416f.
154. Yang Z., Hao X., Chen S., Ma Z., Wang W., Wang C., Yue L., Sun H., Shao Q., Murugadoss V and Guo Z.: Long-term antibacterial stable reduced graphene oxide nanocomposites loaded with cuprous oxide nanoparticles. J. Colloid Interface Sci. 533, 13 (2019).
155. Yang, H.-M.; Lee, H. J.; Jang, K.-S.; Park, C. W.; Yang, H. W.; Heo, W. D.; Kim, J.-D.J. Mater. Chem. 2009, 19, 4566.
156. Yang, H.-M.; Lee, H. J.; Park, C. W.; Yoon, S. R.; Lim, S.; Jung, B. H.; Kim, J.-D. Chem. Commun. 2011, 47, 5322.
157. Yang, L., Tian, J., Meng, J., Zhao, R., Li, C., Ma, J. and Jin, T., "Modification and characterization of Fe_3O_4 nanoparticles for use in adsorption of alkaloids", Molecules, Vol. 23, No. 3, (2018), 176–185.
158. Yang, S., Zeng, T., Li, Y., Liu, J., Chen, Q., Zhou, J., Ye, Y. and Tang, B., "Preparation of graphene oxide decorated Fe_3O_4@ SiO_2 nanocomposites with superior adsorption capacity and SERS detection for organic dyes", Journal of Nanomaterials, Vol. 16, No. 1, (2015), 1–8.
159. Yao, Y., Miao, S., Liu, S., Ma, L. P., Sun, H. & Wang, S. 2012. Synthesis, characterization, and adsorption properties of magnetic Fe_3O_4:graphene nanocomposite. Chem. Eng. J. 184, 326–332.
160. Yavuz, C.T., Mayo, J.T., Yu, W.W., Prakash, A., Falkner, J.C., Yean, S., Cong, L., Shipley, H.J., Kan, A., Tomson, M., Natelson, D., Colvin, V.L., 2006. Low-Field Magnetic Separation of Monodisperse Fe_3O_4 Nanocrystals. Sci. 314(5801), 964– 967. http://doi.ord/10.1126/science.1131475.
161. Yu, J.; Kiwi, J.; Wang, T.; Pulgarin, C.; Rtimi, S. Duality in the Mechanism of Hexagonal ZnO/CuxO Nanowires Inducing Sulfamethazine Degradation under Solar or Visible Light. Catalysts 2019, 9, 916.

162. Yu, L., Wu, H., Wu, B., Wang, Z., Cao, H., Fu, C. and Jia, N., "Magnetic Fe_3O_4-reduced graphene oxide nanocompositesbased electrochemical biosensing", Nano-Micro Letters, Vol. 6, No. 3, (2014), 258–267.
163. Zhang H, Xie AJ, Wang CP, Wang HS, Shen YH, Tian XY. Room temperature fabrication of an RGO-Fe_3O_4 composite hydrogel and its excellent wave absorption properties. RSC Advances. 2014;4(28):14441-14446.
164. Zhang Y., Yang Y., Dong Z., Shen J., Song Q., Wang X., Mao W., Pu Y., Li X., J. Mater. Sci. Mater. Electron. 2020, 31, 15007.
165. Zhang Z., Dou M., Liu H., Dai L., Wang F., Small 2016, 12, 4193.
166. Zhang, Y., Tang, Y., Li, S., Yu, S., Chem. Eng. J. 2013, 222, 94–100.
167. Zhao G, Mo Z, Zhang P, et al. Synthesis of graphene/ Fe_3O_4/NiO magnetic nanocomposites and its application in photocatalytic degradation the organic pollutants in wastewater[J]. Journal of Porous Materials, 2015, 22/5: 1245-1253.
168. Zhao, G., Song, S., Wang, C., Wu, Q., Wang, Z., Anal. Chim. Acta 2011, 708, 155–159.
169. Zhou GM, Wang DW, Li F, et al. Graphene-wrapped Fe_3O_4 anode material with improved reversible capacity and cyclic stability for lithium ion batteries. Chem Mater. 2010; 22(18): 5306-5313.
170. Zhou W., Tang K., Zeng S and Qi Y., Nanotechnology, 19(6), (2008), DOI:10.1088/0957-4484/19/6/065602.